Enhancing phase change material performance through the incorporation of thermally conductive objects at the solid-liquid interface

by

J.(José) Amigo

to obtain the degree of Master of Science in Mechanical Engineering
at Delft University of Technology,
to be defended publicly on Friday August 30, 2024 at 15:00.

Student number:	5715679	
Project duration:	January 1, 2024 – August 30, 2024	
Track:	Energy, flow and process technology	
Thesis committee:	Prof. dr. K. Hooman,	TU Delft, supervisor
	Dr. E. Zanetti,	TU Delft
	Dr. R. Delfos,	TU Delft
	Dr. B.J. Boersma,	TU Delft

TU Delft Delft University of Technology

Abstract

Latent heat storage using phase change materials (PCMs) is a promising technology for storing and recovering waste heat. PCMs offer high energy density and can be tailored for specific melting temperatures, making them suitable for various applications, including temperature stabilization in buildings and thermal management of electronics and batteries. However, a significant disadvantage of PCMs is their low thermal conductivity, which slows the process of charging and discharging thermal energy. This work explores a novel approach to enhance the melting rate of PCMs by incorporating thermally conductive objects (TCOs) within the PCM. The TCO density lies between the solid and liquid PCM densities and is designed to follow the solid-liquid interface. First, an analytical model based on the Stefan problem formulation and a numerical model developed using Ansys Fluent, with locally modified thermal conductivity at the solid-liquid interface, were created to simulate the thermal behavior of the PCM with the addition of TCOs. An experimental setup, consisting of a rectangular enclosure with an organic paraffin as the PCM and hollow aluminum cylinders as the TCOs, was employed to validate these models under purely conductive melting conditions, with heating from the top and cooling from the bottom. Experimental results indicate that the addition of cylinders increased the melting rate by 19% under purely conductive conditions compared to the scenario without cylinders. However, the cylinders enhanced heat flux only within the first 12 mm, beyond which the thermal resistance of the liquid PCM became dominant, preventing further heat flux improvements. During solidification, the cylinders did not move with the solid front and were engulfed at the bottom. In the second part of this work, the developed Fluent model is used to study hypothetical scenarios where a TCO is added to the PCM, but heating comes from the side walls and melting is driven by convection. In this scenario, the inclusion of a TCO at the solid-liquid interface acts as a moving fin, increasing the melting rate by 62% and enhancing thermal power dissipation from 26.5 W to 75.4 W. Future research should focus on experimentally validating this scenario under convective melting, exploring methods to mechanically return the TCO to its starting position for repeatability, and conducting an energy analysis to determine whether the benefits of an enhanced melting rate outweigh the energy required to move the object and the increased manufacturing costs of the latent heat storage system.

Acknoledgements

I would like to express my gratitude to my supervisor, Kamel Hooman, and my co-supervisor, Emanuele Zanetti, for their support, time and feedback throughout the project.

I would also like to thank everyone who supported me in the lab with guidance, materials, and equipment. This includes Bart Hoek, Rene Delfos, Jasper Ruijgrok, Teus Westeneng, and Edwin Overmars.

Lastly, I would like to thank Valentina, as well as my family and friends, for their constant support and for being with me throughout this academic journey.

Contents

Chapter 1

Introduction

1.1 Context

If we take a look at the world's energy consumption in 2022, fossil fuels had a share of 63% and direct usage of electricity 22%, with 28% of it coming from renewable energy. After the Paris Agreement was signed, the energy sector has a challenging road map if we intend to limit the global temperature increase below 1.5^oC by 2050. At present, power generation stands as the largest contributor to carbon dioxide emissions, but at the same time it is the leading sector in the transition to net zero emission, by enabling the integration of renewable energy sources. Hence, a crucial aspect of this road map involves boosting electricity's contribution to 65% of the energy sector, with 91% of it coming from renewable energy [1].

According to the International Energy Agency [2], heating is the world's largest energy end use, accounting for almost half of the global final energy consumption (219 EJ). The two main applications demanding for heat are industrial processes, with a share of 53% of total heat consumed, and space and water heating for buildings, with a 44%. However, the heating sector is largely dominated by fossil fuels, contributing to 39% of energy-related CO_2 emissions in 2022 (14.1 Gt CO_2). Based on the 2022-2027 energy projections, heating consumption, excluding ambient heat harnessed by heat pumps, is expected to grow 6 % (14 EJ), but only 14% is expected to come from renewable energy by 2027.

In this context, there is an urgent need of having a more efficient heat management if we intend to reduce CO_2 emissions significantly. All energetic losses eventually get converted to low-grade heat and therefore, waste heat represents the major source of recoverable loss in energy usage. In the study of [3], a quantification of global waste heat for the year 2030 and their impact on CO_2 emissions was made for different energy scenarios. In the scenario where legislation remained the same from 2016 onwards, 51.5% of energy would end up in waste heat. On the other hand, if we intended to limit the average global temperature increase by 2^oC by 2100, waste heat would represent 49.3%. Regardless of the case, it becomes evident that there is a substantial potential in optimizing heat utilization through the deployment of energy-recovery and storage devices, such as heat exchangers, heat pumps and thermal energy storage systems (TES). According to the International Renewable Energy Agency (IRENA), TES has the potential to be a relevant enabler of increased renewable penetration in the energy system, by making them more stable, flexible and cheaper to build and operate [4].

1.2 Thermal energy storage

TES can store heat or cold to be used later under varying conditions such as temperature, place or power [5]. These systems become useful in situations where the energy production is intermittent, by enabling the release of heat when the demand surpasses the production, or by storing the excess of heat for future use when the production surpasses the demand [6]. This allows decoupling supply and demand of heat and cold. TES also make the usage of thermal energy more efficient, by enabling recovery of heat from industries or components that produce waste heat during their operation [7]. TES covers a wide range of technologies, which are normally classified into three main categories (Figure 1.1): sensible heat storage (SHS), latent heat storage (LHS) and thermochemical storage (TCS) [5, 6].

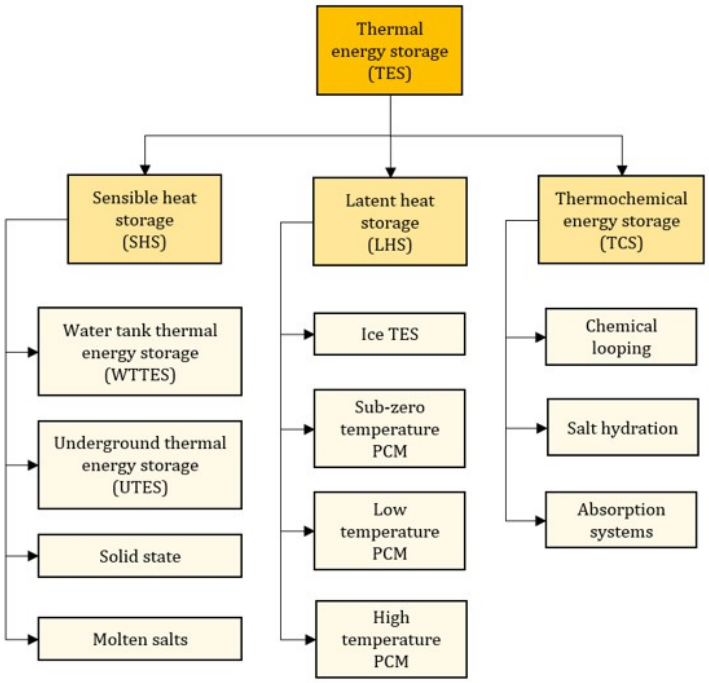

Figure 1.1: TES types and main technologies. Elaborated with information from [4].

1.2.1 Sensible heat storage (SHS)

In SHS, thermal energy is stored in a material by increasing its temperature and the stored heat is recovered as the material cools down, without changing its phase [8]. Due to its simplicity and low cost, it is by far the most widely used technology and can be found in various applications, including the power sector, residential hot water storage and space heating, industry and district heating and cooling [7]. Some examples of SHS technologies are water tank thermal energy storage (WTTES), solid-state thermal storage, molten salts and underground thermal energy storage (UTES) [4]. Depending on the application, they can be designed to operate anywhere between -150-1000 ^oC. However, its main disadvantages are given by its low energy density (0.4-0.9 kWh/m^3), which implies requiring large volumes to store the storage material and greater losses of thermal energy throughout the charge and discharge cycles [9, 10]. The amount of heat stored or released in the storage medium, Q, is proportional to the temperature difference between the storage material and the application,ΔT, and the thermal capacity of the material (mC_p), according to the following equation [5, 9].

$$Q_s = m \cdot c_p \cdot \Delta T \tag{1.1}$$

1.2.2 Latent heat storage (LHS)

In LHS, heat is transferred as a result of a phase change that occurs in a specific narrow temperature range of the material [9]. Materials used for LHS are called phase change materials (PCM). In case of a solid-liquid example, during the melting process of the PCM, heat is absorbed and during the solidification process, heat is released [5]. These systems are characterized for having a high energy density (50-80 kWh/m^3), negligible temperature change throughout the charge and discharge cycle and a moderate cost [10]. Nowadays, a wide variety of PCMs with different melting temperature ranges have been developed [11]. Depending on the temperature range, technologies can be grouped into sub-zero PCMs ($< 0^oC$), ice (0^oC), low-temperature PCMs (0-120^oC) and high-temperature PCMs ($> 120^oC$). These characteristics make them suitable for a wide variety of applications, such as solar thermal systems, buildings, heat recovery, cooling of electronics and power batteries [12]. The amount of heat stored or released is proportional to the enthalpy difference between the solid and liquid phase, ΔH_l, and the PCM mass, m, as described by the following equation [9].

$$Q_l = m \cdot \Delta H_l \tag{1.2}$$

1.2.3 Thermochemical energy storage (TCS)

Lastly, in TCS, energy is stored in endothermic chemical reactions and released at any time by promoting the reverse exothermic reaction. These systems are characterised for having the highest energy density among TES units and having a high exergetic efficency [9]. Another advantage of TCS is that they can store heat for long periods at environmental temperatures without the need of heavy insulation and consequently, they have become a widely researched technology for low temperature applications like buildings heating and cooling [13]. TCS, similarly to the other TES systems, involves three main processes, charging, storing and discharging. During the charging process, the thermochemical material absorbs energy from the working fluid, resulting in a endothermic process and the dissociation of the material. During the storing process, the products of this reaction are separately stored. Lastly, in the discharging process, the working fluid absorbs energy from the thermochemical material in a exothermic process and the the material recombines to start the cycle again [14]. TCS can be classified into sorption-based and reversible reaction-based energy storage [4]. Sorption-based TCS have a temperature range that goes from 0 to 105^oC and some common materials are silica gels, alumina-silicates, metal-organic frameworks and composite sorbents. Reaction-based TCS instead, have a broader range of temperatures, going from 0 to 250^oC, they have a higher energy density and a wider availability of materials, including salt hydrates, metal hydides, fertilizer-based salts and magnesium oxides [13]. The amount of heat stored or released is proportional to the reaction enthalpy, ΔH_r, and the number of moles, n_A, according to the following equation.

$$Q_t = n_A \Delta H_r \tag{1.3}$$

All TES have weaknesses and strengths relative to each other. In terms of maturity, SHS and LHS, have both commercially available technologies. In SHS, UTES and WTTES have been widely used in district heating and cooling applications. Some examples are the 23715-m^3 WTTES installed in the power plant Diemen 34, with a capacity around 1800 MWh, or the larger scale 30-MW aquifer thermal energy storage (ATES) at TU/e Eindhoven [15]. Another commercially mature technology in SHS, are molten salts for power generation. Gemasolar (19.9 MW) in Spain and Cerro Dominador (110 MW) in Chile are some examples of thermosolar plants. Molten salts are used both as heat transfer fluid and storage medium [16], with heat coming from solar radiation and reaching temperatures of up to 560^oC in the hot salt tank. According to [4], in LHS systems, only sub-zero PCMs are currently at a commercial level, whereas high-temperature PCMs and low temperature PCMs are still at demonstration and prototype phases, respectively. This difference in maturity among PCMs can be explained due to the fact that water is the most common PCM and has been used for cooling food and beverages already for a long time. Some examples of companies developing ice thermal storage tanks for buildings and district cooling are BAC, Calmac and Cristopia, accounting for 23.5 GWh of thermal storage capacity altogether in 2015 [17]. The charging process is done with chillers that use renewable energy to freeze water and the discharging is done by an additional heat transfer fluid as water or glycol. However, according to other authors [18], multiple low- and high-temperature PCMs have already been used in commercial products for years. In building materials, some examples are the micro-encapsulated PCMs integrated plaster boards (Knauf) or the floor heating and cooling roofs systems developed by PCM Technology. In building space heating, an example are the heat batteries developed by Sunamp. These consist in a container completely filled with PCM and with the use of an internal heat exchanger for water, heat is exchanged with the PCM. In medical applications, they can be found in heat cushions for heat and cold therapeutic treatments (Rubitherm GmbH) or in neonatal treatment applications used for helping premature babies maintain their body temperature (PCM Technology). Another application is the thermal management of batteries and other electronics devices, with examples such as AllCellTech and their battery package enclosure made of composite PCM. Despite the various examples of high and low temperature PCMs in market, their usage is usually limited or available on request.

Figure 1.2: Commercially available PCM technologies. (a) Ice thermal storage tanks from Calmac for building cooling. (b) UniQ Heat battery from Sunamp, used to increase the energy density of a domestic water heater. (c) Battery package enclosure developed by AllCellTech for battery thermal management.

In case of TCS, technologies are still at a demonstration phase in absorption systems, and prototype phase in salt hydration systems [4]. An example of the former, is the LiBr-water absorption prototype built by [19], which could store 8 kWh of heat and produce a heating power of 1 kW. This system uses a concentrated solution of LiBr refrigerant to absorb water and release heat in the process. The charging step is done by adding heat to the solution and vapor off the water. According to the review of absorption systems for TES done by [20], there is still more research needed for their implementation and future research should focus on improving the heat exchangers, developing new configurations for integrating them with chillers and heat pumps, and finding new pairs of absorbent and absorbate without freezing and rectification issues.

In terms of costs, SHS is expected to be between 0.1-25 usd/kWh by 2030, LHS between 60-90 usd/kWh and TCS between 80-160 usd/kWh. At large scale, SHS are the preferred option by the market, due to their lower cost and simplicity. However, LHS and TCS are particularly attractive in thermal regulation and energy saving applications where space is limited, because of its higher energy density and small temperature range for charging and discharging heat [21, 22, 23] . Some examples are the thermal management of temperature-sensitive components such as batteries [24] and electronic devices [11] and temperature control in buildings by providing heating and cooling [21].

1.3 Phase change materials

1.3.1 Classification

Phase-change materials can be classified into different categories: based on their phase state, based on their chemical composition and based on their melting temperature range [11]. In terms of phase state, PCMs used in industry can be found in various phase transitions, such as solid-solid, solid-liquid and liquid-gas states [24]. However, solid-liquid PCMs are the most common and therefore, particular attention will be given to this category in this work.

1.3.1.1 Chemical composition

In terms of chemical composition, PCMs can be classified into organic, inorganic and eutectic. Organic PCMs are mainly composed of three groups of substances: paraffins, fatty acids and organic mixtures. Among these, paraffins are the most studied. Some of the characteristics of organic PCMs are being chemically and thermally stable, non-corrosive, having limited supercooling, no phase segregation, recyclable, having a high latent heat of fusion ($110 - 280\ kJ/kg$) and a relatively low melting point ($<100^oC$) [11, 25]. Their main drawbacks are given by their low thermal conductivity (0.1-0.3 W/m K), high flammability, high volume expansion during phase transition and being incompatible with polymer containers [9, 21, 26]. To address their flammability, the addition of flame retardants has demonstrated to be an effective mitigation technique, with materials like hydroxides [27], ammonium polyphosphate [28] and expanded graphite [29].

On the other hand, inorganic PCMs, usually consist in hydrated salts or metals. One of the most commonly used salt hydrates is sodium sulfate decahydrate. In comparison to organic PCMs, they are characterized for having higher thermal conductivity (0.5-0.6 W/m K), higher melting point (25-140 ^oC), higher latent heat of fusion (110-280 kJ/kg) and lower cost [4, 9]. However, their main drawbacks are being

corrosive, having sub-cooling, thermal instability and segregation. Some examples of the methods found in literature to mitigate these undesired properties, are the addition of expanded graphite to reduce sub-cooling [30] or mixing with other salts to reduce phase separation [31].

Eutectic PCMs are homogeneous mixtures that can be composed of two or more organic and inorganic PCMs (organic-organic, inorganic-inorganic or organic-inorganic). Taking a simple case of a binary mixture, the eutectic point represents the mixture that has the minimum melting point. The components of this mixture are completely miscible in liquid phase and completely inmiscible in solid phase and therefore, crystallize as pure substances [32]. Eutectics are normally tuned to have a desired melting point and latent heat, so they have the potential to match specific applications needs better. Additionally, due to their congruent phase transition, they do not suffer from segregation, allowing them to have multiple heating and cooling cycles with the same performance [33]. However, they are still at the research phase and therefore more development is needed for them to have a competitive market price [21].

1.3.1.2 Melting temperature

There is currently no clear consensus in literature regarding the categorization of PCMs based on temperature ranges. As mentioned earlier in this work, according to IRENA [4], four ranges can be defined based on the type of technology. The first range is formed by sub-zero PCMs, goes from -100 to 0^oC and is composed by eutectic water-salt solutions and non-eutectic water-salt solutions. Most of the research around sub-zero PCMs is focused on eutectic water-salt solutions, due to their higher latent heat of fusion and broader temperature range [34]. A broad review of different sub-zero PCM materials, both commercial and experimental, can be found in the work of [35], with melting temperatures that go from -1 to -114^oC. Depending on the sub-zero temperature range, they can be used for cold air distribution (-5^oC), liquefaction of propane (-42^oC) or for low temperature climatic chambers (-70^oC). The second temperature range is given by ice, at 0^oC, which despite being a single material, is the most widely used PCM. The third temperature range is given by low temperature PCMs, and goes from >0 to 120^oC. In this range we can find most of organic and inorganic PCMs. Some authors [9] divide this temperature range into two, grouping building heating and cooling applications at the lower end, and solar and thermal management applications at the higher end. The fourth and last temperature range goes from 120^oC and above, and consists in binary or ternary eutectic mixtures of salts. Some common compounds for these mixtures are nitrate, carbonate and sulphate salts of alkali or alkaline metals, such as potassium, lithium and calcium [36]. This category of PCM is particularly relevant for energy intensive processes, including applications such as distillation, nitrate melting, dyeing and hydrogen production [25].

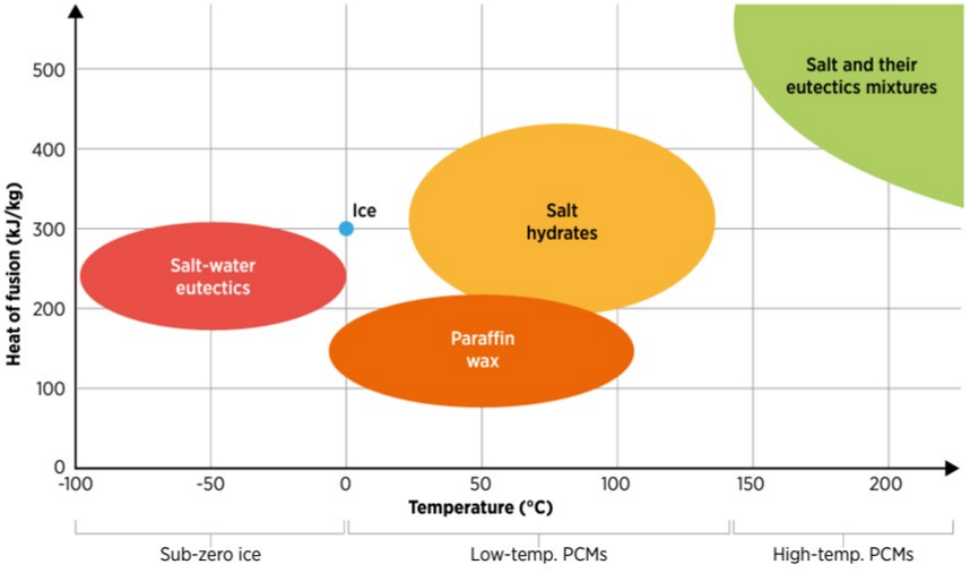

Figure 1.3: Thermal properties of PCMs based on their chemical composition [4].

Depending on the application and type of material, there are different considerations to take into account when storing PCMs. A more detailed overview of the different methods for storing PCMs will be presented in the next sub-section.

1.3.2 Storage methods

PCMs can be found in market as either pure materials or encapsulated. Regardless of the case, when used in practical applications, they are encased within a finite shell. According to [36], LHS containers can be divided into compact and encapsulated.

Compact LHS are characterised for enclosing the PCM within a larger container with an embedded heat exchanger. In case of LHS with simultaneous charging and discharging, some common heat exchanger geometries are flat plate heat exchangers, multi-layers heat exchangers, multi-tube heat exchangers, triplex-tube heat exchangers and plate-and-tube heat exchangers (Figure 1.4). This type of LHS is usually found in heating and cooling supply applications [37]. The advantage with respect to encapsulated PCMs, is having a higher thermal power and better thermal response. This can be explained due to their larger heat transfer area and because the HTF is active, i.e. it is forced to move with a pump, resulting in a higher heat transfer coefficient. However, as part of the PCM is replaced by the heat exchanger, the higher thermal power comes with the trade-off of having a lower energy density. Another drawback for compact systems, is given by the fact that PCMs contained in larger volumes are more prone to phase segregation [22].

On the other hand, encapsulated LHS, are those systems in which the PCM is contained within small containers and the heat exchange with the HTF occurs through the outer shell. Encapsulation of PCMs is a common practice to prevent their leakage to environment, minimize phase separation and prolong their lifetime [9]. Depending on their length scale, they can be categorised in macro-encapsulation ($> 1\ mm$) and micro-encapsulationn ($1\ \mu m - \ 1\ mm$). Different encapsulation materials, such as acrylic resin, polyurea, silica, and alumina, have been employed, and they are selected based on their compatibility with the PCM and the mechanical demands of the particular application [33]. In this type of storage systems, the HTF can be either passive (driven by natural convection) or active. Passive systems, are usually found in applications for temperature control (e.g. macroencapsulated PCM in bags for building's walls).

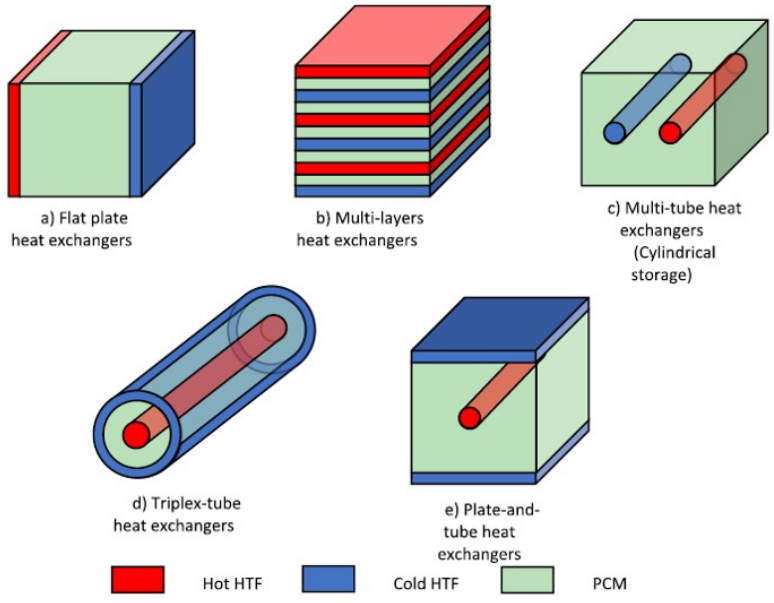

Figure 1.4: Heat exchanger geometries used in LHS with simultaneous charging and discharging [6].

1.3.3 Modeling techniques

The study of PCMs and design of LHS units, often requires mathematical models to describe the thermal behaviour of materials. Having a good understanding of the heat transfer in melting and solidification processes allows evaluating whether the thermal capacity of a PCM will meet the requirement of an application or if the temperatures will stabilize within a certain limit [37]. Some of the most cited models in literature are the analytical solution to the Stefan problem [38] and the numerical model based on the enthalpy-porosity formulation of Voller [39].

1.3.3.1 Stefan problem

The Stefan problem is based on a 1-dimensional semi-infinite layer of PCM occupying the space $0 < x < \infty$, with a melting temperature T_m. If we consider the solidification of this PCM, the complete domain is initially at liquid phase at the phase change temperature T_m. Then, the temperature at x=0 is changed to T_0 and kept constant for t>0, as shown in Figure 1.5.

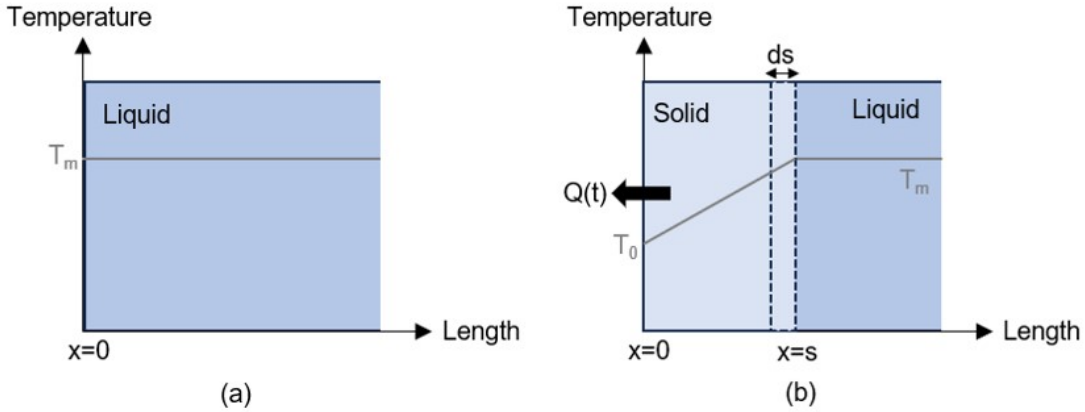

Figure 1.5: Solidification process according to the Stefan problem. (a) t=0, (b) t>0.

Some of the assumptions of this model are that solidification occurs isothermally and without supercooling at a temperature of T_m, the thermal properties are isotropic, the heat transfer occurs only by conduction and heat is stored only as latent heat [37]. Convection and sensible heat storage are therefore negligible. The amount of heat released as the solid front moves is given by latent heat and can be calculated as:

$$\frac{dQ(t)}{dt} = (h_l - h_s)\frac{dm}{dt} = (h_l - h_s)\rho_s A\frac{ds(t)}{dt} \tag{1.4}$$

Where h_l and h_s are the liquid and solid enthalpy, respectively, ρ_s is the solid phase density and $ds(t)/dt$ is the speed at which the front is moving. On the other hand, heat conduction across the moving front can be calculated as:

$$\frac{dQ(t)}{dt} = k_s A\frac{T_m - T_0}{s(t)} \tag{1.5}$$

Where k_s is the thermal conductivity of the solid phase, T_m is the temperature at the right side of the front, equal to the melting temperature, and T_0 is the temperature at the left side of the front. Equalizing equations (1.4) and (1.5), the following equation can be derived.

$$(h_l - h_s)\rho_s A\frac{ds(t)}{dt} = k_s A\frac{T_m - T_0}{s(t)} \tag{1.6}$$

Then, using separation of variables in space s and time t, and integrating from $t' = 0$ to $t' = t$, the location of the solid front s can be calculated as a function of time:

$$s(t) = \sqrt{\frac{2k_s(T_m - T_0)t}{\rho_s(h_l - h_s)}} \tag{1.7}$$

Despite the restrictions of this model given by the previous assumptions, it is still useful for doing initial estimates and study the influence of parameters, such as the heat transfer coefficient, on the time it takes a solid front to move in a 1-D geometry [37].

1.3.3.2 Enthalpy-porosity method

The enthalpy-porosity method is currently the most used technique for studying heat transport problems involving phase transitions [10]. This model, unlike the Stefan problem, does not track the phase interface directly and uses a modified energy equation, based on enthalpy and temperature. A quantity called liquid fraction, λ, is defined for each cell in the PCM domain and varies from 0, for a completely solid phase, to 1, for a completely liquid phase, according to the following equation.

$$\lambda = \begin{cases} 0, & T < T_s \\ \frac{T - T_s}{T_l - T_s}, & T_s \leq T < T_l \\ 1, & T \geq T_l \end{cases} \tag{1.8}$$

Where T_s is the solidus temperature, the temperature below which the material is completely solid, and T_l is the liquidus temperature, the temperature above which the material is completely liquid. The total enthalpy of the material is calculated as the sum of the sensible enthalpy, h, and the latent heat, ΔH (Equation 1.9). Additionally, the latent heat can vary between zero, for a solid, and the latent heat of fusion, L, for a liquid.

$$H = h + \Delta H \tag{1.9}$$

$$h = h_{ref} + \int_{T_m}^{T} c_P dT \tag{1.10}$$

$$\Delta H = \lambda L \tag{1.11}$$

The phase transition region, called mushy zone, is modeled as a porous zone and flow is governed by Darcy's law, with porosity being equal to the liquid fraction. Using equations (1.8)- (1.11), the governing equations for describing the heat transfer in the PCM domain can be defined, and are given by continuity (1.12), momentum (1.13) and energy (1.14):

$$\nabla \cdot \vec{v} = 0 \tag{1.12}$$

$$\rho \frac{\partial \vec{v}}{\partial t} + \rho(\vec{v} \cdot \nabla)\vec{v} = -\nabla P + \mu \nabla^2 \vec{v} + \rho \beta g (T - T_m) + \vec{S} \tag{1.13}$$

$$\frac{\partial (\rho H)}{\partial t} + \nabla \cdot (\rho \vec{v} H) = \nabla \cdot (k \nabla T) \tag{1.14}$$

Where ρ, $\vec{v}$, μ, P, β, g and t are density, velocity, dynamic viscosity, pressure, thermal expansion coefficient, gravity and time, respectively. Additionally, a sink term $\vec{S}$ is included in the momentum equation. This term takes a value of zero in a completely liquid phase to allow free motion, but it slows down the flow as the liquid fraction decreases, freezing the flow completely when the PCM is in solid phase. The sink term can be calculated as:

$$\vec{S} = \frac{-(1-\lambda)^2}{\lambda^3 + \varepsilon} A_{mush} \vec{v} \tag{1.15}$$

Where ε is a small number ($10^{-2} - 10^{-3}$) to prevent division by zero and A_{mush} is the mushy zone constant, used to measure the amplitude of velocity damping in the mushy region. In most of the cases, this parameter is calibrated to match experimental data. However, its value can vary widely depending on the PCM used or the geometry of the enclosure, taking values that can go from 10^5 to 10^{15} [40]. In the study of [41], a numerical model was used to see the impact of varying A_{mush} between 10^5 and 10^7 in the melting and solidification process of lauric acid. They showed that higher values of A_{mush} lead to a decrease of the convective strength, resulting in a slower melting process. Yang et al. [42] instead, provided a physical insight of the mushy zone by experimentally analyzing the microstructure of paraffin wax during phase transition. They found that the microstructure evolves quite differently during melting and solidification, and the characteristic length of the particles in the interphase liquid is smaller during solidification. Using empirical correlations, they proposed an equation for the mushy zone constant as a function of the dynamic viscosity of the PCM and the particle's diameter ($A_{mush} = 180\mu/d^2$). Despite the highly non-linear behaviour of A_{mush}, they still argued that for modeling the macro-scale thermal behavior of PCMs, it is a reasonable approach to use an average value for A_{mush}.

One of the main limitations of the enthalpy-porosity model is given by its incapability of modeling situations in which the solid phase is completely surrounded by the liquid phase and therefore, is free to move [43]. This situation is known as close-contact melting (CCM) and the motion of the solid phase allows the melting process to occur faster. In the work of [44] for example, CCM was achieved by heating the outer shell of a double-pipe concentric unit with a longitudinally finned inner tube. The experimental results showed that when the solid phase was detached from the walls and was free to move, the melting time was shortened by a factor of 2.5. Extensions of the enthalpy-porosity model are currently being developed to capture CCM [45]. However, in the vast majority of cases, the current enthalpy-porosity model has been successfully validated with experiments [10, 46, 47, 48, 49, 50] and it is used in most of the computational fluid dynamic (CFD) softwares, such as Ansys Fluent, COMSOL and OpenFOAM.

1.3.4 PCM performance

1.3.4.1 Figures of merit

According to [37], the ideal PCM should meet a set of requirements that can be grouped into physical, technical and economical aspects, as shown in the table below.

Physical	Technical	Economic
- Suitable temperature for the application. - Large phase change enthalpy. - Cycle stability / repeatability. - Small amount of subcooling. - High thermal conductivity.	- Low vapor pressure. - Small volume change during phase transition. - Chemical and thermal stability. - Compatibility of the PCM with the enclosure. - Safety and environmental constraints.	- Low cost. - Recyclable.

Table 1.1: Phase-change material requirements.

However, most of the studies referring to PCM's performance have focused in two thermophysical properties: having a high thermal conductivity, to have a faster thermal response, and having a high thermal capacitance, to have a higher energy density [23]. To address these characteristics and compare different materials, multiple figures of merit (FOM) have been proposed in literature [11, 23, 51]. Shamberger et al. [51], based on the analytical solution of the two-phase Neumann-Stefan problem, showed that the following expression was proportional to the heat transfer between the PCM and the surrounding medium: [11].

$$FOM_1 = \sqrt{k\rho L_h} \tag{1.16}$$

Where k, ρ and L_h are the thermal conductivity, the density and the latent heat of the PCM, respectively. In other words, the bigger this FOM, the faster the thermal response of the PCM to the temperature input [11]. It is important to note that FOM_1 is limited to the thermophysical properties of the PCM and does not consider parameters such as the geometry of the domain, melting point and boundary conditions. To address these additional parameters, Tripathi et al. [23] defined a timescale based FOM as a function of three characteristic timescales: the time for melting (t_{melt}), the time for heat to diffuse (t_{diff}) and the time it takes the temperature to increase before the melting begins (t_{sens}).

$$FOM_2 = FOM_1 \cdot \frac{t_{melt}}{t_{sens} + t_{diff}} \tag{1.17}$$

The different timescales were calculated using the following equations.

$$t_{diff} = \frac{L_c^2}{5\alpha}, \quad t_{sens} = \frac{mc_P(T_m - T)}{P}, \quad t_{melt} = \frac{mL_h}{P} \tag{1.18}$$

Where L_c, α, m, c_p, L_h and P are the characteristic length scale of the geometry, thermal diffusivity of the PCM, total mass of PCM, specific heat of the PCM, latent heat of the PCM and thermal power input, respectively.

Another alternative to assess the performance of LHS is to use a more industry-based approach. Conventional heat exchanger analysis methods, like $\varepsilon - NTU$ or $LMTD$ are not suitable for evaluating LHS due to the transient nature of the charging and discharging of heat in PCMs [52]. In the study of [53], to compare the performance of LHS units with different amount of fins, they used the mean power ($\dot{Q}_{mean}$) as a comparative metric, defined as the average of the heat transfer over the energy stored in the system (E).

$$\dot{Q}_{mean} = \frac{\int Q dE}{E} \tag{1.19}$$

1.3.4.2 Melting process

Taking any of the previous performance definitions into account, one of the critical parameters for improving these systems is having a higher heat transfer rate between the PCM and the heat transfer fluid (HTF), which is exchanging heat with the PCM. This can be challenging considering the thermal conductivity of PCMs is normally low. To have a better understanding of the role of conduction in the melting process of PCMs, we will use as an example a rectangular enclosure with a constant heat flux coming from the left side-wall (Figure 1.6). As [54] explains it, we can expect the melting process to begin with a pure conduction mode (phase I), followed by a natural convection mode (phase II). In phase I, we can expect the isotherms to

be parallel to the heating wall, indicating that the dominant heat transfer mechanism is conduction. Despite the low thermal conductivity of PCMs, the highest heat transfer coefficient can be expected in this phase, because only a thin film separates the heat source from the solid PCM and therefore the thermal resistance is low. In phase II, as the liquid phase increases, the warmer liquid PCM will tend to go to the top of the enclosure through a convective driven-flow, deflecting towards the solid-liquid interface and resulting in a higher melting rate at the upper part of the enclosure [12]. The heat transfer coefficient is relatively constant in this phase, because the higher thermal resistance of the growing layer of liquid is balanced with the intensification of the convective-driven flows. As the solid-liquid interface decreases and the solid phase shrinks to the bottom corner, conduction becomes more dominant. Wang et al. [55] used two stages to describe this last part of the melting process, one moderate convection stage and one weak convection stage. Since both of these phases have in common a decreasing heat transfer coefficient, they will be grouped in a single phase for simplicity, called phase III. Unlike phase I, which is also dominated by conduction, phase III has a high thermal resistance due to the relatively stagnant liquid surrounding the solid phase, resulting in a low melting rate. In the experimental work of [12] for example, approximately half of the time was used to melt the last 20% of solid phase of a rectangular enclosure heated from one side. Therefore, the practical consequence of having a low thermal conductivity, lies in the fact that LHS units require longer times to completely charge and discharge thermal energy [47]. To address this problem, numerous studies have focused in developing methods for enhancing the heat transfer of PCMs. The following sub-section will review the main techniques found in literature.

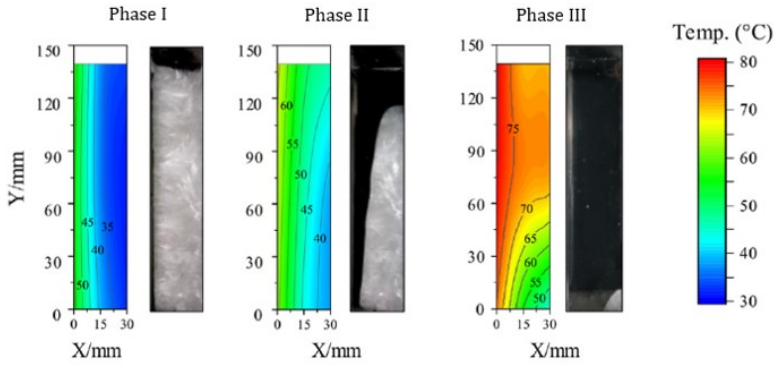

Figure 1.6: Melting process of a PCM inside a rectangular enclosure under constant heating from the left wall [54].

1.3.5 Methods for improving the heat transfer

Among the different alternatives for improving the heat transfer of LHS, the predominant focus lies in increasing the contact area between the PCM and the HTF using high conductive materials, with methods such as: adding fins, metal foams or adding nano-particles. It is important to note that all of these techniques involve substituting part of the PCM with materials which normally have a lower energy storage capacity, which means there is always a trade-off between improving the thermal response and improving the energy density of LHS units [47].

1.3.5.1 Fins

The addition of fins is the most common method to enhance the heat transfer rate between two mediums, due to its simplicity and effectiveness. It has been widely studied in traditional heat exchangers as well as in LHS, with various shapes (rectangular, cylindrical, spherical), dimensions (lenght,thickness) and configurations [11]. To demonstrate the benefits of adding fins to a LHS, it is a common practice to compare the performance of the LHS with and without fins. Yang et al. [56] used a triplex-tube heat exchanger with annular fins around the inner tube to study the fin dimensions that could minimize the melting time. Their results showed that the addition of fins could potentially reduce the melting time in 65% in comparison to the melting time without fins. A similar study was done by Mat et al. [48] using radial fins under three scenarios: when the fins were placed at the exterior of the inner tube, when they were placed at the interior of the outer tube and when they were placed at both surfaces. The study showed that irrespective of the scenario, the melting time was decreased 57% when fins were added. Sciacovelli et al. [49] showed that radial fins could be further optimized by using tree-shaped fins. When fins had two bifurcations, the melting time was 24% lower than the case with single radial fins. Other studies instead, have analyzed non-uniform distributions of

fins and the impact of their location on the melting rate. Mahdi et al. [47] modeled a horizontally oriented triplex heat-tube exchanger to analyze the relevance of the different heat transfer mechanisms when fins were placed at the lower and upper part of the inner tube. Using a dimensionless analysis they showed that the contribution of natural convection in the melting process was 170% and 40% higher than conduction in the upper region and lower regions, respectively. Based on this observation, they demonstrated that less and shorter fins are more helpful on the upper region, as they allow vortices caused by natural convection to fully develop. In the lower region instead, where conduction had a greater relevance, having more and longer fins was better. Various studies [10, 12, 46, 50] have come up with a similar conclusion: due to the thermal stratification during the melting process of PCMs, placing fins at the lower colder regions has a greater effect in reducing the melting time. As [12] explains it, the thermal stratification on top of a fin tends to be unstable; cold denser layers of PCM lie on top of warm lighter layers. This results in a buoyant driven vortex flow. On the other hand, below a fin, thermal stratification is stable; warm lighter layers of PCM lie on top of cold denser PCM, and therefore the heat transfer is dominated by conduction. The practical consequence for LHS units heated from one side, is that fins can enhance the melting rate significantly in comparison to a situation without fins during most of the melting process, but it may still take long to melt the bottom corner described previously as phase III (Figure 1.3). In the work of [46] for example, they modeled a rectangular PCM enclosure with uniformly distributed fins on the heating side-wall, and showed that melting the first 20% of the PCM took 4.8% of the time of the melting process, whereas melting the last 20% took 67% of the time.

1.3.5.2 Metal foams

Other techniques, as adding metal foams or nano-particles to PCMs, have gained attention in the last years, due to the fact they allow a more uniform melting and solidification process, in comparison to fins, by uniformly increasing the effective thermal conductivity of PCMs. Metal foams used in PCM applications are open-cell metal foams with a large number of interconnected and randomly oriented pores [11]. Metal foams allow the heat input to quickly be transferred through the solid matrix by conduction, enhancing the thermal response of LHS [26]. Zhang et al. [57] used a numerical model to study the melting process of paraffin with an embedded aluminium metal foam, to see the effect the porosity had on the energy density and the heat transfer rate. Four scenarios were modeled: three cases with uniform porosity (85.9, 91.3 and 95.8%) and one case with a linear porosity gradient, going from 95.8% at the top to 85.9% at the bottom. Their analysis showed that among the uniform-porosity cases, there was a positive linear correlation between energy density and porosity. The average heat transfer rate instead, increased abruptly for the case with the lowest porosity, because conduction was the dominant heat transfer mechanism, allowing a faster melting rate in the lower part of the PCM. However, an even better heat transfer rate was achieved when a metal foam with a porosity gradient was used, as it allowed convection to develop in the upper half of the PCM.

1.3.5.3 Nanoparticles

Lastly, the addition of nanoparticles usually consist in metals, oxides or carbon particles [11]. Similarly as with metal foams, there is trade-off between enhancing the effective thermal conductivity of the PCM by adding more nano-particles and enhancing the energy density. Zeng et al. [58] experimentally studied the effect of adding Ag nano-wires to tetradecanol. As the Ag volume fraction increased from 0 to 11.8%, the thermal conductivity of the composite PCM increased from 0.32 W/mK to 1.46 W/mK and the latent heat decreased from 220 kJ/kg to 76.5 kJ/kg. This trade-off was also shown in the work of [59], where a numerical model was used to study the effect of adding Al_2O_3 nanoparticles to three different PCMs at concentrations ranging from 2 to 10% in volume fraction. Their results showed that when the volume fraction was 10%, the melting time decreased in 31.6-38.0%. However, this melting rate enhancement was accompanied by a decrease in energy and exergy storage in 40.6% and 39.8%, respectively. The authors showed that the addition of the first 5% of Al_2O_3 was responsible for decreasing the melting time in 29.6-35.8%, whereas the last 5% only decreased the melting time an additional 2.0-2.2%, clearly showing a diminishing return concerning the decrease in melting time as the volume fraction of nanoparticles increased. The reason for this is that as nanoparticles concentration increase, there are more agglomerations and layering of fluid molecules on the surface of nano-particles, resulting in a higher viscosity and density for the composite PCM [60]. As a result, a higher buoyancy force is required to overcome the resistance of viscous forces, limiting the heat transfer through natural convection [61, 62].

Chapter 2

Research goal

Regardless of the heat transfer enhancing technique used for PCMs, the incorporation of conductive materials yields the highest benefits in the regions where conduction is a relevant heat transfer mechanism [57, 61, 62, 63]. When the liquid fraction starts to increase and natural convection becomes the dominant heat transfer mechanism instead, the inclusion of solid materials can negatively affect the melting rate by obstructing convection vortices. In the light of this context, the goal of this thesis is:

To develop an innovative method for improving the melting process of phase change materials by incorporating thermally conductive objects capable of tracking the solid-liquid interface and locally increase the thermal conductivity.

The implementation of this solution can be done by designing small solid objects, whose density lies between that of the solid and liquid phases of the PCM. This solution would allow increasing the thermal conductivity locally at the mushy zone, decreasing the thermal resistance of this region and enhancing the heat transfer between the liquid and solid phases. This method can potentially allow a more uniform melting rate throughout time, because it would accelerate the melting of the solid fraction that usually remains on the bottom corner as described earlier in phase III of Figure 1.6. On the other hand, the buoyant-driven heat transfer at the liquid phase would not be obstructed by the thermally conductive objects (TCO) as they would lie at the bottom boundary of the liquid region. The assessment of this solution will be done using Ansys Fluent and results will be validated with an experimental setup. Based on the previous review and to the authors' knowledge, there are no studies up to date reported in literature that have worked on a similar method for enhancing the melting rate of PCMs.

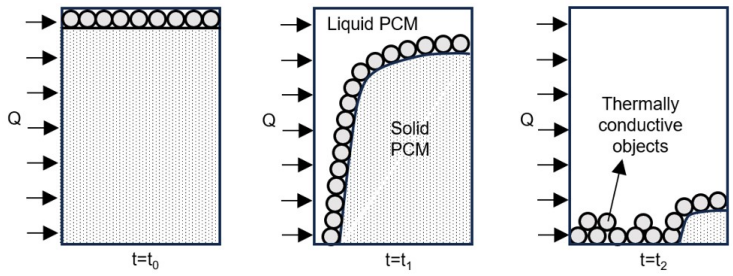

(a) Heating applied on the left wall.

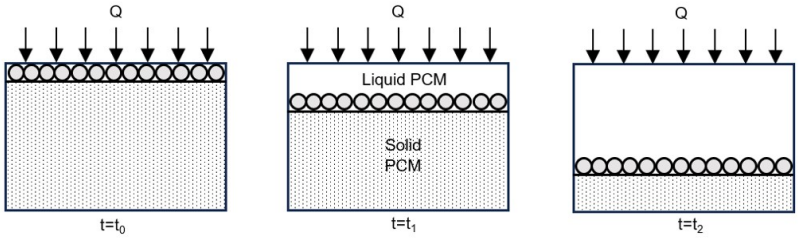

(b) Heating applied on the top wall.

Figure 2.1: Melting of the PCM with the addition of thermally conductive objects.

Some of the main challenges and questions this work aims to answer are the following.

(i) What is the optimum shape, size and material for the TCOs?

The material should meet two requirements: having a thermal conductivity as high as possible, to enhance the melting rate of the PCM, and having a density that is between the liquid and solid density of the PCM, to allow the TCO to sink as the PCM melts and float as the PCM solidifies. Considering the density of commercial PCMs is usually between 800-1900 kg/m^3, examples of materials that would meet these requirements are closed-hollow metals and ceramics. To ensure a TCO floats during the PCM solidification process, it is crucial that the majority of the particle's volume fraction resides within the mushy zone. The reason for this is that if the TCO's density is between that of the solid and liquid PCM, the only fluid region in which buoyancy would be greater than the weight of the TCO is the mushy zone. As a result, we can expect the size of the TCO to have a similar order of magnitude than the mushy zone thickness. Since manufacturing and testing multiple types of materials can be time consuming and more expensive, most of the evaluation of this solution will be through computational models and the experiment will be used as a validation case.

(ii) How much will the melting rate improve?

To quantify the improvement of the melting rate when adding TCOs to a PCM, a base case without TCOs will be used for comparison. Some of the metrics considered for this comparison are mean power, energy density and melting time. Experimental and simulation results will be used to address this question.

(iii) Is the melting and solidification process repeatable?

This question is particularly challenging because it implies that solid objects must return to their original positions during the solidification process. One significant obstacle in achieving repeatability is the potential engulfment of the solid objects within the solid PCM. This issue can arise, for instance, if the PCM experiences phase segregation, leading to an unexpected density distribution. Another factor could be the clustering of TCOs. For example, if two TCOs cluster together, the combined weight might exceed the buoyancy force, causing the bottom TCO to become engulfed in the solid PCM. Understanding the distribution of TCOs during both the melting and solidification processes is a crucial part of the experimental findings.

Chapter 3

Methodology

3.1 Overview

In this chapter, the computational methods and experiment used to study the melting and solidification behavior of a PCM with and without the addition of TCOs is presented.

For simplicity, this study will consider a rectangular enclosure for the PCM. The TCOs are intended move together with the solid-liquid interface and their density must be greater than the liquid PCM, but smaller than the solid PCM. As a result, they are expected to sink in the liquid PCM, but float in the mushy zone, the region in which the liquid fraction lies between zero and one. To have liquid phase forming on top of the solid phase, two configurations are possible in terms of where the heat is applied.

In the first case, heat is applied on one of the side walls. As mentioned earlier, the heat transfer between the heating surface and the solid PCM will be initially dominated by conduction, but as the liquid fraction increases, convection will become the dominant heat transfer mechanism. The solid-liquid interface is initially expected to be vertical. However, as convection occurs, the interface will likely curve and tend toward a more horizontal orientation. Despite convection accelerates the melting process, the fact that the liquid-solid interface is not horizontal can bring an additional challenge, as the TCOs will tend to agglomerate, as shown in Figure 2.1a. In the second case, heat is applied on the top surface and therefore, a stable thermal stratification is expected to occur as warmer PCM will lie on top of colder denser PCM. In this case, heat transfer will be driven by conduction throughout all the melting process and due to the low thermal conductivity of PCMs, it will be a slower process in comparison to the first case. This case not ideal for practical applications as thermal charging and discharging will take longer, but it represents a simpler scenario to study in an experiment as the liquid-solid interface will be horizontal and therefore we can expect no, or a minimum agglomeration between TCOs, as shown in Figure 2.1b. Given the lack of previous studies on both cases, this work will focus on the second case for the experimental setup, as it presents a simpler scenario for studying the TCO's motion. However, both cases will be analyzed using computational models.

3.2 Experiment

3.2.1 Components

The following section present the different equipment, measurement techniques and procedures used to obtain experimental data. A schematic view of the main components of the experimental setup is shown in Figure 3.4. These can be grouped into the (1) PCM enclosure, (2) the thermal bath, (3) the data acquisition system with the thermocouples and the (4) camera setup.

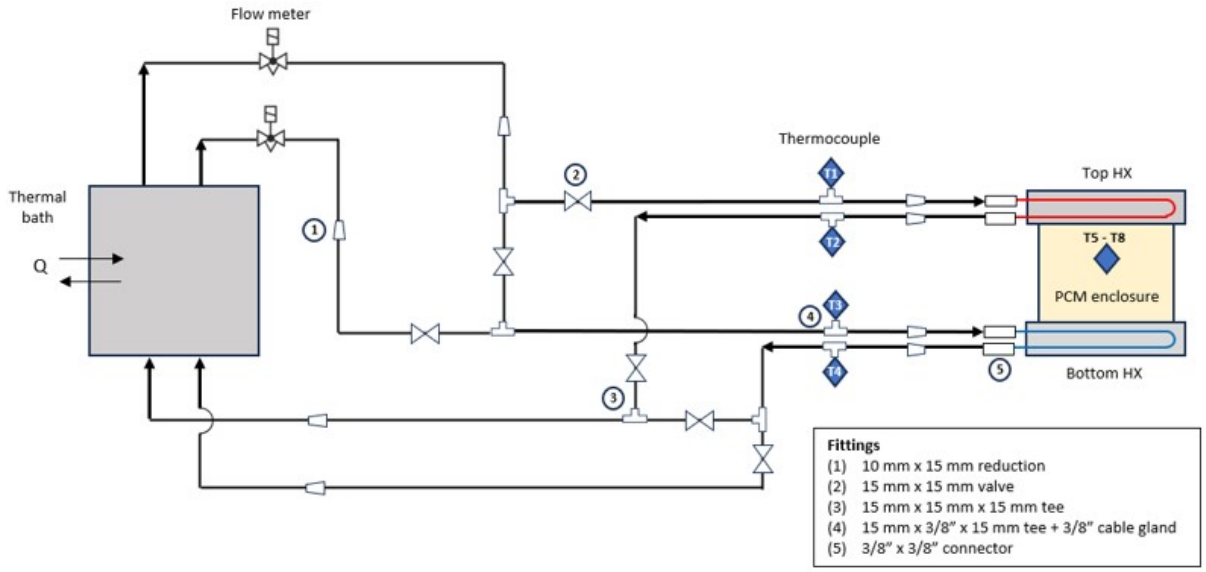

Figure 3.1: Schematics of the PCM experiment.

An organic PCM was chosen for this experiment due to its less corrosive behavior in comparison to hydrated salts. The organic PCM used for this work was OM29 from the company Pluss, which has a melting temperature of 28^{o}C. More details of the thermal properties of OM29 are shown in Table 3.1.

Property	Value (liquid / solid)
Phase transition temperature (^oC)	28 / 25
Latent heat (kJ/kg·K)	194 / 188
Density (kg/m^3)	870 / 976
Specific heat (J/kg·K)	2710 / 2320
Thermal conductivity (W/m·K)	0.172 / 0.293

Table 3.1: OM29 thermal properties, based on Pluss datasheet.

Since the density of the PCM lies between 870 and 976 kg/m^3 for the liquid and solid phases, respectively, the target density for the TCOs was defined as the average of these two values, equal to 923 kg/m^3. Additionally, the TCO will only be pushed by the mushy zone during solidification, if the buoyancy force exerted by the mushy zone is greater than the weight of the particle. If we assume density varies linearly through the mushy zone as a function of temperature, the previous statement can only be true if the size of the TCOs is equal or smaller than the mushy zone thickness. However, up to date, there is not a consensus in literature on how to predict the mushy zone thickness. The characteristic length of the mushy zone during solidification and melting is different due to the different way in which the microstructure evolves in each of these processes [42]. According to [64], the maximum length of the mushy zone has an inverse relation with the Biot number, Stefan number and thermal diffusion. Some of the practical consequences of this relation is that it increases with time and higher heating or cooling rates, results in smaller mushy zone thicknesses. In the work of [64], the reported mushy zone thickness varied from 0 to 22.5 mm during their solidification experiment. On the other hand, in the work of [65], the mushy zone thickness varied from 0 to 7.2 mm during their melting experiments. For the purposes of this work, the selection of the TCO will assume a mushy zone thickness equal to 5 mm. To meet the target size and density for the TCOs, hollow aluminium tubes of 5 mm outer-diameter, 0.45 mm wall thickness and 90 mm lenght were used (Figure 3.2). Additionally, to cover the ends of the tubes, two PETG plugs were 3D printed, consisting in 4.1-mm diameter cylinders with a length of 2.2 mm. Taking aluminium, PETG and air density as 2700, 1230 and 1.293 kg/m^3 respectively, and using Equation 3.1, the theoretical density for each cylinder is 924.7 kg/m^3.

The table below summarizes the weight, volume and density of one cylinder.

$$\rho_p = \frac{m_{Al} + m_{air} + m_{PETG}}{V_{Al} + V_{air} + V_{PETG}} \tag{3.1}$$

Parameter	Symbol	Value
Aluminium mass	m_{Al}	1563 mg
Air mass	m_{air}	1.5 mg
PETG mass	m_{PETG}	87.7 mg
Aluminium volume	V_{Al}	0.58 cm^3
Air volume	V_{Al}	1.19 cm^3
PETG volume	V_{PETG}	0.07 cm^3

Table 3.2: OM29 thermal properties, based on Pluss datasheet.

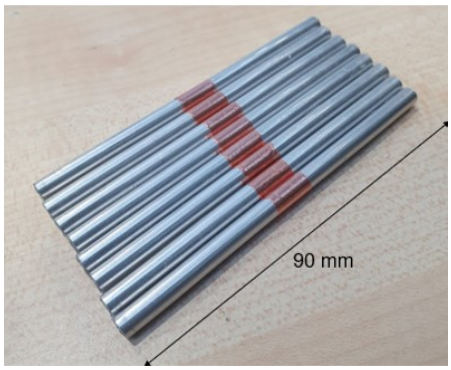

Figure 3.2: Hollow aluminium cylinders used in the experiments.

The PCM was contained within a plexiglass box of 100 mm x 100 mm x 50 mm in length x width x height and a thickness of 4 mm. As mentioned in the earlier section, to have a more controlled motion of the melting and solidification front, heating was applied from the top of the enclosure and cooling from the bottom of the enclosure. Two tubed cold plates from Wakefield Thermal, model 120456, were used to provide a relatively uniform temperature at the top and bottom surfaces of the PCM. These heat exchangers consist in an aluminium plate of 152 mm x 127 mm x 15 mm in length x width x height, with an embedded 3/8"-outer diameter copper tube with 4 passes. Water was circulated inside the tubes at 3 l/min (0.79 gpm) at a fixed temperature. Based on the manufacturer's datasheet, these plates have a thermal resistance that varies between 0.021-0.016$^oC/W$ for a water flow rate of 0.5-1.0 gpm and 400 W of heat dissipation. Both plates are in contact with the PCM and 3 holes were drilled on the top heating plate to allow the expansion of the PCM during the melting process. To attach the plexiglass enclosure to the heat exchangers, two 3D printed frames made of ABS were used, together with 8 M3 bolts and an o-ring to prevent leakages of PCM. Figure 3.3 shows the SolidWorks model of the different components mentioned earlier and their assembly. The complete PCM enclosure and the outer faces of the heating and cooling plates are insulated with 2 cm of polystyrene foam, with a density of 25 kg/m^3.

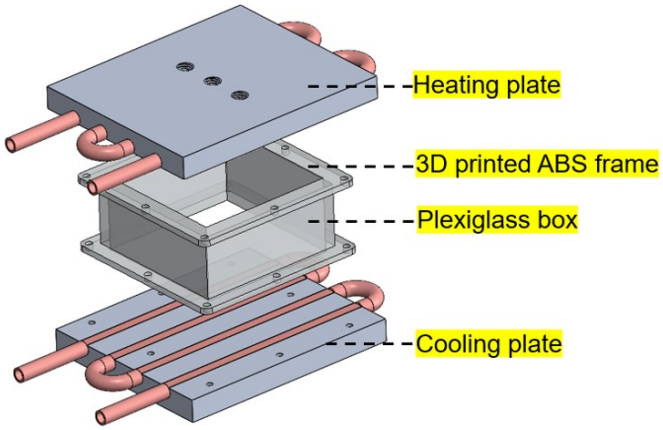

Figure 3.3: SolidWorks model for the PCM enclosure.

A general overview of the experimental setup, including the PCM enclosure and the cold and hot thermal baths, is shown in Figure 3.4a. To provide a relatively constant temperature at the heating plate, the Gunt WL110 HEX unit was used. It has a hot a cold water circuit, each of them equipped with a pump and a flow control system that allows having a flow rate between 0.3 and 3 l/min. The hot water circuit is equipped with a 10-liters thermal bath and an electric heater which has a power output of up to 3 kW and allows controlling the hot water temperature between 10 and 70^oC. Two thermocouples, at the inlet and outlet of the thermal bath and a temperature controller are used to supply heat to the water tank and have a constant temperature throughout time. Since the Gunt WL110 unit was not equipped with a chiller and the cold water circuit was connected to the laboratory mains which had a variable temperature between 15 to 18^oC, a separate unit, Lauda Proline RP845, was used instead to provide a water at lower temperatures. To connect the heating and cooling plates to the cold and hot thermal baths, a 12-mm outer diameter PEX tubing circuit was used. During the experimental tests, a GoPro Hero 8 Black was used to capture pictures of the PCM from one side of the enclosure, as shown in Figure 3.4b. The EPS insulation on the wall adjacent to the camera was only removed for short periods before each picture was taken. To improve the visibility of the solid-liquid interface inside the enclosure, a 45 mm $\times$ 86 mm white LED module (Adafruit 1621) was placed on the outer face of the wall opposite the camera.

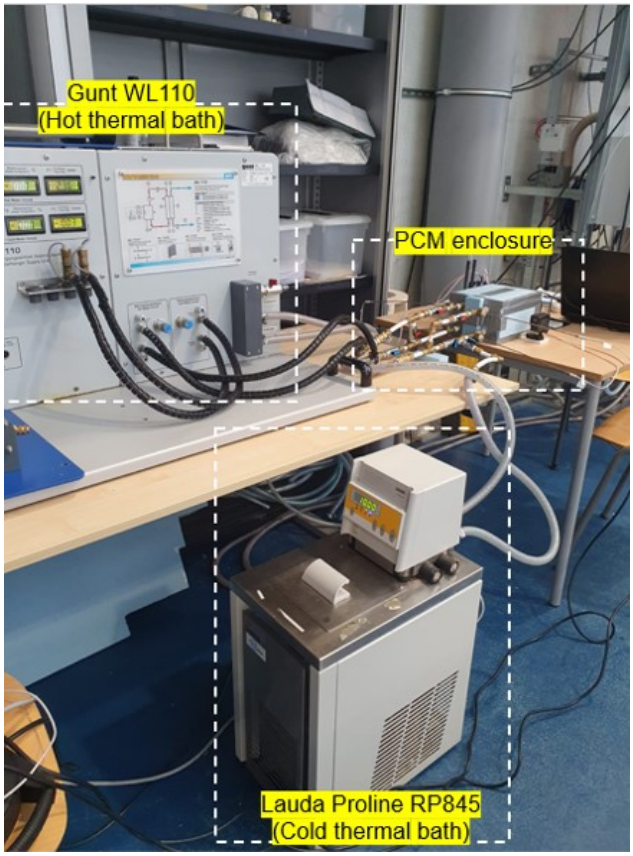

(a) Thermal baths and PCM enclosure.

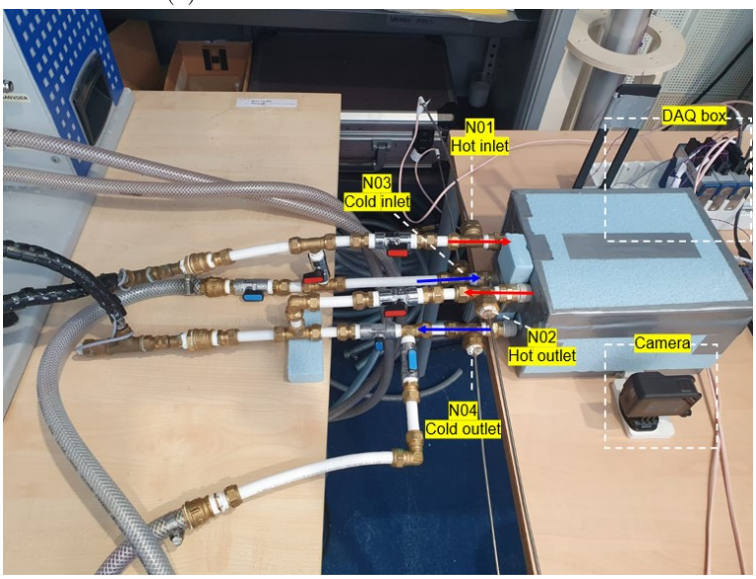

(b) N-type thermocouples, DAQ box and camera positioning.

Figure 3.4: Experimental setup overview.

3.2.2 Measurement techniques

3.2.2.1 Overview

The sensors used in the experimental setup consist of four N-type and six T-type thermocouples, two paddle-wheel flow meters, DS8031 from Bürkert, and one weight scale, Mettier PE12. The N-type thermocouples were placed at the inlets and outlets of the heating and cooling plates, as shown in Figure 3.4b, and were used to have an estimation of the average temperature on each plate. The T-type thermocouples were attached to a PETG 3D printed component at the center of the PCM enclosure, at five different heights, as shown in Figure 3.5. The PETG component was attached to one of the plate heat exchangers with two

nylon plugs. Even though there is direct contact between this component and the heating or cooling source, heat conduction is expected to be similar to that with the PCM. This is because the thermal conductivity for PETG and nylon, which falls within the range of 0.15-0.25 W/m K, is close to the thermal conductivity of OM29 (Table 3.1). Additionally, the reminding T-type thermocouple did not have a fixed position. Instead, it was used to monitor the temperature at different points, e.g. air, outer side of the copper pipe, EPS foam. The analogue signals from the thermocouples were collected and processed into digital data using three NI9211 data acquisition boxes from National Instruments. Additionally, a script in LabVIEW 2017 was used to visualize and store temperature throughout time with a sampling frequency of 3 Hz.

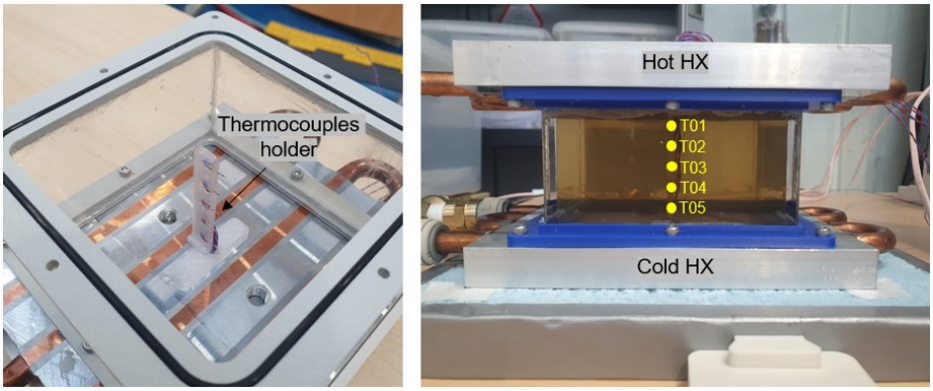

Figure 3.5: T-type thermocouples positioning.

The flow meter was placed at the outlets of the hot thermal bath, and was used by the Gunt WL110 unit to control the flow rate. However, these measurements were not stored in time and only real-time data was available for flow rate. Lastly, the weight scale was used to indirectly measure the PCM mass used in each experiment, by subtracting the mass of the complete enclosure with PCM by the mass of the complete enclosure without PCM. The weight of the particles was also measured to verify whether their density was within the design range.

Among the different measured quantities, temperature and mass were directly obtained with the thermocouples and the weight scale, respectively. However, heat flux was estimated indirectly and therefore error propagation from derived quantities was considered for the uncertainty estimation. If we consider a result R, which is a function of N independent variables x_1,...,x_N, defined as:

$$R = f_1\{x_1, x_2, ..., x_N\} \tag{3.2}$$

Each variable will contain a certain value of uncertainty ($u_{\overline{x}_i}$) which can be converted into uncertainty in R (u_{R_i}) by using the following relation [66]:

$$u_{R_i} = \left(\frac{\partial R}{\partial x_i}\right)_{x=\overline{x}} u_{x_i} \tag{3.3}$$

Finally, the contribution of all the uncertainties can be calculated using the root sum squared method (RSS):

$$u_R = \sqrt{\sum_{i=1}^{N} {u_{R_i}}^2} \tag{3.4}$$

3.2.2.2 Uncertainty

Before running the main tests, the uncertainty of the sensors was estimated to ensure more reliable results. The uncertainty of the thermocouples was determined as a combination of the bias (u_b) and random errors (u_r) using the RSS method. To estimate these errors, repeated measurements of a known temperature were conducted. The thermocouples were submerged in a bucket of ice, with careful attention to placing the thermocouple's hot junction on the solid ice, not in the melted water beneath it, to ensure the actual temperature was 0°C. For each thermocouple, data was collected for 30 seconds at a sampling rate of 3 Hz, five different times, resulting in five samples of 90 data points each. Using this data, the mean temperature of the five samples, T_{mean}, was calculated, and the difference between T_{mean} and the known temperature, T_{ref}, was used to calculate the bias error of each thermocouple:

$$u_b = T_{mean} - T_{ref} \tag{3.5}$$

On the other hand, the random uncertainty was estimated at a 95% confidence level, assuming a normal distribution of the temperature data points and considering a normal distribution of the means of the samples, according to the following equation:

$$u_r = t_{v,p}\frac{s_x}{\sqrt{N}} \tag{3.6}$$

where $t_{v,p}$ is the student parameter, equal to 2.77 (v=4, p=95%), N are the number of samples and s_x is the standard deviation of the samples [66]. The uncertainty of the weight scale instead, was directly obtained from the manufacturer's datasheet. Table 3.3 summarizes the total uncertainty obtained for the different sensors. More details about the uncertainty analysis of the thermocouples can be found in the Appenddix A.

Sensor	Type/Model	Location	Uncertainty
Thermocouple 1	N	Hot plate inlet	$\pm 0.32^o$C
Thermocouple 2	N	Hot plate outlet	$\pm 0.29^o$C
Thermocouple 3	N	Cold plate inlet	$\pm 0.35^o$C
Thermocouple 4	N	Cold plate outlet	$\pm 0.44^o$C
Thermocouple 5	T	PCM (z = 1 cm)	$\pm 0.31^o$C
Thermocouple 6	T	PCM (z = 2 cm)	$\pm 0.21^o$C
Thermocouple 7	T	PCM (z = 3 cm)	$\pm 0.16^o$C
Thermocouple 8	T	PCM (z = 4 cm)	$\pm 0.06^o$C
Thermocouple 9	T	PCM (z = 5 cm)	$\pm 0.05^o$C
Thermocouple 10	T	Copper pipe	$\pm 0.16^o$C
Weight scale	Mettier PE12	N/A	±0.5 g
Flow meter	DS8031 Bürker	N/A	±0.01 l/s

Table 3.3: Thermocouples and weight scale uncertainties.

The uncertainty of the heat fluxes can be calculated as a function of the uncertainties in temperature differences and the mass flow rate. Using equation 3.3, we can translate the mass flow rate (u_m), and temperature difference ($u_{\Delta T}$) uncertainties into the heat flux uncertainty as:

$$u_Q = \sqrt{\left(\frac{\partial Q}{\partial m}u_m\right)^2 + \left(\frac{\partial Q}{\partial \Delta T}u_{\Delta T}\right)^2} \tag{3.7}$$

Table 3.4 summarizes the uncertainties for temperature difference and heat fluxes at the hot and cold plates. For these calculations, water density and specific heat are taken as 1000 kg/m^3 and 4184 J/kg K,respectively, and ΔT is considered to be negligible. After 10 minutes of operation at the target cooling or heating temperatures, the experimental heat flux is expected to be below 10 W. This implies that the uncertainty in the heat flux measurement is approximately an order of magnitude greater than the expected heat flux. Due to this significant uncertainty, the mass flow rate was not recorded. Instead, it was set to the maximum flow rate of the thermal bath, 3 l/min, to maintain the temperature as uniform as possible at the heat exchangers.

Variable	Uncertainty
ΔT hot plate	$\pm 0.43^o$C
ΔT cold plate	$\pm 0.56^o$C
Heat flux hot plate	$\pm$90.25 W
Heat flux cold plate	$\pm$117.51 W

Table 3.4: Uncertainty of estimated quantities.

3.2.3 Experimental procedures

3.2.3.1 Material preparation and mounting procedure

This section outlines the procedure employed to prepare the setup for conducting the melting and solidification tests. The objective of this standardized procedure is to ensure consistent initial conditions regarding temperature and PCM mass, thereby enabling the comparison of different tests.

- The plexiglass box, along with the top and bottom heat exchangers, was mounted using M3 steel bolts. Five thermocouples are placed inside plexiglass enclosure at different heights, separated by 1 cm from each other. To keep them in place, they were glued to a 3D printed component, which was attached to one of the heat exchangers, as shown in Figure 3.5. The entire assembly was then weighed on a digital weight scale.
- The heat exchanger with the attached thermocouples is used as the top or bottom heat exchanger depending on the test. During the melting test, it is used as the top heating plate, whereas during the solidification test, it is used as the bottom cooling plate. The reason for having the thermocouples at a known distance from the heating or cooling plates, is given by the fact that these plates represent the initial position of the melting and solidification fronts, respectively.
- After weighing the empty enclosure, the top heat exchanger was removed to allow filling the plexiglass with PCM.
- In case the melting or solidification test procedures were run with hollow-aluminium cylinders within the PCM, these were added on top of the bottom heat exchanger, before pouring the PCM, as shown in Figure 3.7. Because the thermocouple holder was in the midsection of the heat exchanger, this part, approximately 1 cm in width, was left without cylinders. To maintain symmetric conditions, 8 cylinders were added on each side of the thermocouple holder.
- A separate container is filled with solid PCM cut into smaller pieces to increase the heat transfer area and accelerate the melting process. The container was then placed in a bath of warm water until the PCM was fully melted.
- The liquid PCM was then poured into the plexiglass box until its level was close to the top of the enclosure.
- The second plate heat exchanger, was mounted on top of the plexiglass box and secured with bolts.
- To remove the air gap between the top heat exchanger and the PCM and ensure a direct contact between them, additional liquid PCM was added through the holes of the heat exchanger using a funnel, until it was approximately 5 mm above the top part of the plexiglass box.
- Lastly, the complete assembly was weighed. The PCM's weight was calculated as the difference between the weight of the enclosure with PCM and the weight of the enclosure without PCM. This mass value was then used as a reference for comparing different experiments.

(a) Plexiglass enclosure without PCM.

(b) Plexiglass enclosure with PCM.

Figure 3.6: Weight scale used to measure the plexiglass enclosure mass.

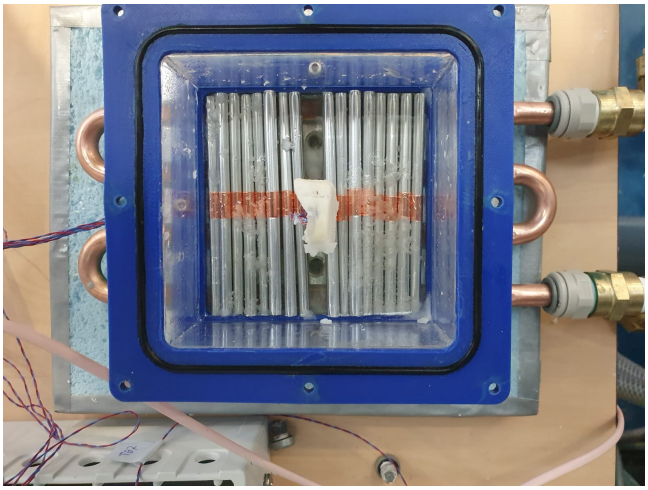

Figure 3.7: Cylinders are added at the bottom of the empty plexiglass enclosure.

The following steps varied depending on whether the melting or solidification test was carried out and therefore will be detailed in the following subsections.

3.2.3.2 Melting test procedure

After the mounting procedure was completed, the PCM was allowed to cool down at ambient temperature until it was completely solidified. As the PCM shrinks during solidification, air gaps may form between the top heat exchanger and the solid PCM, increasing the thermal resistance between them. To minimize this effect, the orifices of the top heat exchanger were covered with plugs, and the entire assembly was inverted. In this new position, the plugs of the heat exchanger, now on the top, were removed to allow the PCM to expand. The melting test procedure can be divided into the preheating phase and the melting phase.

During the preheating phase, the top and bottom heat exchangers were connected to the thermal bath and water was recirculated at 25^{o}C with a flow rate of 3 l/min, as shown in Figure 3.8a. This phase was maintained until the four thermocouples embedded in the PCM read a temperature of 25^{o}C, ensuring a uniform temperature within the PCM.

Once the preheating phase was completed, the recirculation of water on both top and bottom heat exchangers was stopped. The thermal bath was set to 60^{o}C and once the temperature reached this value, water was recirculated through the top heat exchangers at 60^{o}C and 3 l/min, as shown in Figure 3.8b.

3.2.3.3 Solidification test procedure

After the mounting procedure was completed, the enclosure was kept in the same position, with the aluminium cylinders at the bottom of the enclosure. Similarly as with the melting test, a preheating phase was done to ensure similar and uniform temperature conditions between different experiments. The top and bottom heat exchangers were connected to the thermal bath and water was recirculated at 30^oC and 3 l/min.

After the thermocouples read a temperature of 30^oC, the recirculation of hot water through the top and bottom plate heat exchangers was stopped. Then, the solidification phase begins with cold water being recirculated through the bottom plate heat exchanger at 10^oC and 3 l/min, as shown in Figure 3.8c.

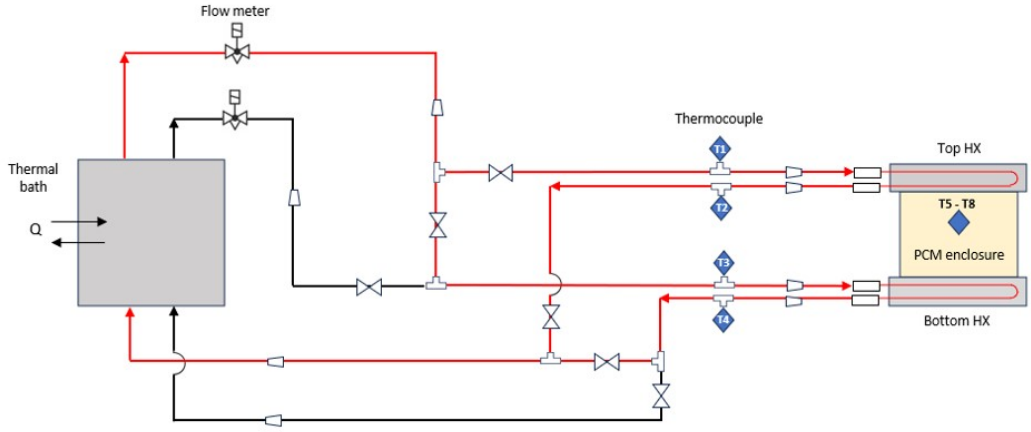

(a) Preheating phase. Q= 3 l/min, T_w=25^{o}C (for melting) or T_w=30^{o}C (for solidification).

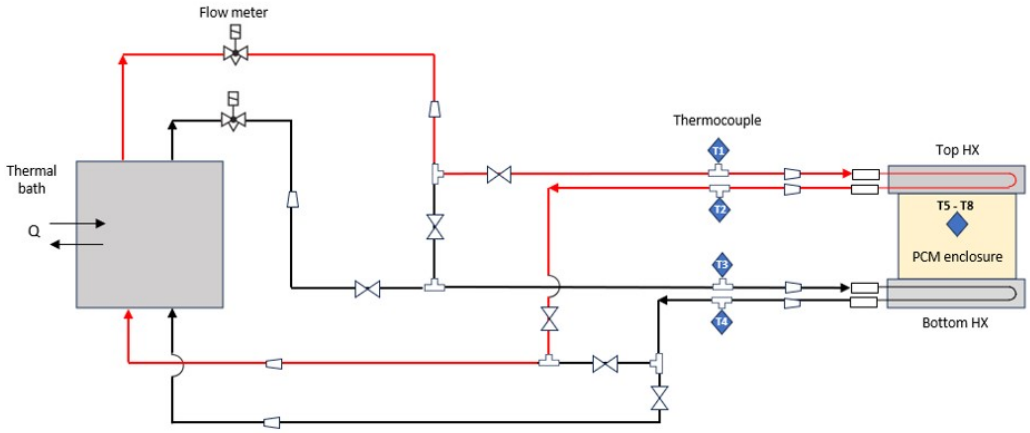

(b) Melting phase. Q= 3 l/min, T_w=60^{o}C.

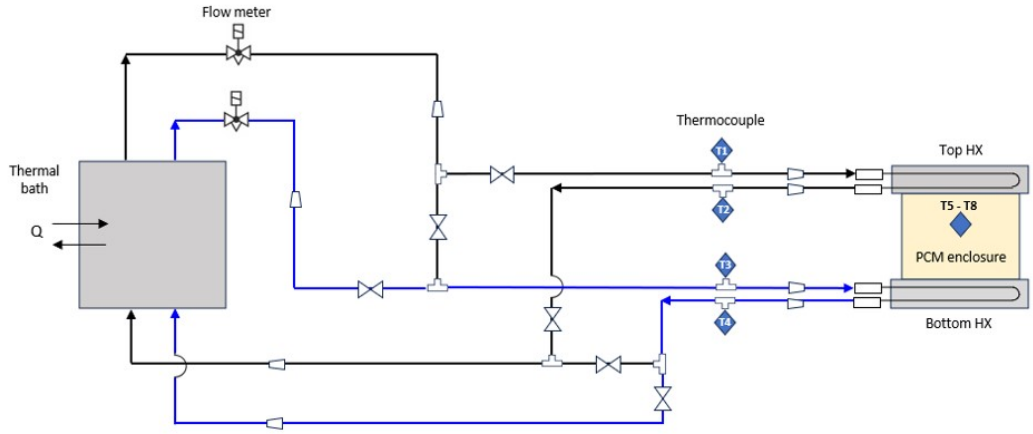

(c) Solidification phase. Q= 3 l/min, T_w=10^{o}C

Figure 3.8: Hydraulic circuit modes of operation.

3.2.3.4 Heat losses test procedure

Despite the PCM enclosure being insulated with polystyrene foam, it is still relevant to measure the heat losses and take them into account in the analysis of the results. The following test was used to obtain the average heat transfer coefficient of the PCM walls. Simililarly as with the melting test, the plexiglass enclosure was filled with PCM following the mounting procedure, cooled down at ambient temperature until it was completely solidified and preheated to 25^{o}C with the insulation around the enclosure. Once the thermocouples embedded in the PCM read 25^{o}C, the recirculation of water through he plate heat exchangers was stopped. The transient temperature inside and outside the enclosure was monitored for 8

hours as the enclosure cooled down. The PCM temperature at time n, T^n_{PCM}, was obtained as the average of the temperatures measured by the five thermocouples. A fifth thermocouple was used to measure the air temperature outside the enclosure at time n, T^n_{air}.

$$T^n_{PCM} = \frac{T^n_1 + T^n_2 + T^n_3 + T^n_4 + T^n_5}{5} \tag{3.8}$$

From conservation of energy, the energy change in the PCM mass (left hand side of equation 3.9) has to be equal to the total heat losses through the walls, Q^n_{wall}. These heat losses can be estimated as the product of the total walls area, A_{tot}, the temperature difference between the PCM and the air, and the average heat transfer coefficient, U_{avg}, given by the right hand side of the equation below:

$$mc_p \frac{(T^{n+1}_{PCM} - T^n_{PCM})}{\Delta t} = Q^n_{wall} \tag{3.9}$$

$$mc_p \frac{(T^{n+1}_{PCM} - T^n_{PCM})}{\Delta t} = U_{avg} A_{tot} (T^n_{air} - T^n_{PCM})$$

where m is the mass of the PCM, and c_p is the specific heat of the solid PCM. Since all quantities are known except for U_{avg}, we can determine the best fit for U_{avg} using the measured data from the 8-hour cooling period.

3.3 Computational analysis

The modeling techniques presented in the previous section 1.3.3 were used to study the phase change process of the PCM in the experiment. First, the analytical solution to the Stefan problem was used to understand the effect of the TCO's thermal properties on the melting time and the thermal power dissipation. Then, to understand the influence of using temperature dependent thermal properties and study additional cases in which convection can be relevant, and therefore the Stefan problem is no longer valid, the enthalpy porosity model of Ansys Fluent was used. As a validation step, both analytical and numerical models were compared to the experimental results.

3.3.1 Analytical model

Since the heat transfer in the experiment is dominated by conduction, the Stefan problem can be used to describe the thermal behavior of the PCM. An additional thermal resistance must be added to include the effect of having a layer of TCOs between the solid and liquid PCM with different thermal properties. If we take the melting process as an example with heat coming from the top, the heat flux from the top wall (T_0) to the solid PCM (T_m) will have to go through two thermal resistances, given by the liquid PCM and the layer of TCOs, as shown in Figure 3.9. The thermal resistance for the liquid PCM, R_{PCM}, will increase with time as the liquid region increases, whereas the thermal resistance for the layer of TCOs, R_{tco}, is constant in time.

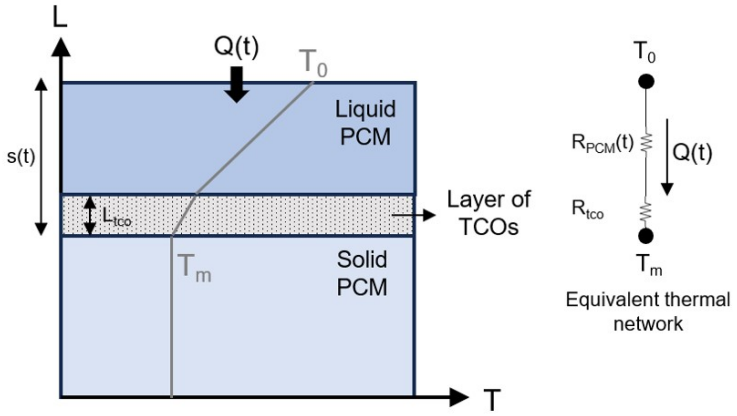

Figure 3.9: Thermal network scheme during the melting process of the PCM.

Besides the assumptions made in the Stefan problem formulation, two additional assumption are made to model the additional layer of TCOs at the solid-liquid interface. First, the TCOs move simultaneously

with the melting and solidification fronts and therefore, they always remain as a horizontal layer, with a thickness L_{tco}, equal to the TCO's height. Second, the liquid PCM between the TCOs is assumed to be part of the layer of TCOs and therefore, the effective thermal properties for this layer take into account both liquid PCM and the TCOs. To compute the thermal resistance of this layer, a 2D-steady state simulation in Fluent was done, as shown in Figure 3.10. The domain consists in a 5-mm width liquid PCM column, with one aluminium tube filled with air inside it. The lateral walls are adiabatic and the top and bottom boundaries have a constant temperature of 303K and 293K, respectively. In steady-state, the heat flux between the top and bottom boundary will be constant. If the heat flux, Q, and the temperature difference between two points, $T_1 - T_2$, are known, we can calculate the thermal resistance between these points as $R_{tco} = (T_2 - T_1)/Q$.

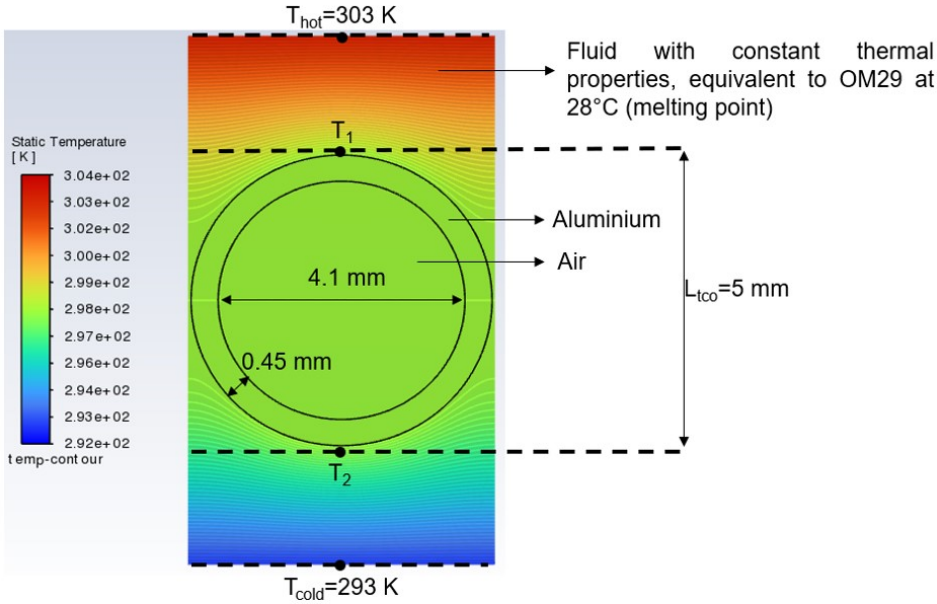

Figure 3.10: Fluent simulation to estimate the effective thermal conductivity of the layer containing the TCO.

Going back to the thermal network of Figure 3.9, and considering R_{pcm} and R_{tco} are two resistances in series, we can rewrite the heat flux equation 1.5 as:

$$\frac{dQ(t)}{dt} = \frac{T_m - T_0}{R_{pcm} + R_{tco}} \tag{3.10}$$

Considering conduction is dominant in this case, the thermal resistances can be calculated as:

$$R_{pcm} = \frac{s(t) - L_{tco}}{k_l A}, \qquad R_{tco} = \frac{L_{tco}}{k_{tco} A} \tag{3.11}$$

Then, following a similar procedure to equations 1.6 and 1.7, we can rewrite the energy balance for a melting volume of PCM as:

$$(h_l - h_s)\rho_s A \frac{ds}{dt} = \frac{T_m - T_0}{R_{pcm} + R_{tco}} \tag{3.12}$$

If we substitute equation 3.11 in equation 3.12, we can obtain a solution for the solid-liquid interface position, $s(t)$, by integrating in time and solving a second order equation, as shown below. It is important to note, that $s(t = 0) = L_{tco}$.

$$s^2 \frac{k_{tco}}{2} + s(L_{tco}(k_l - k_{tco})) - L_{tco}^2(k_l - \frac{k_{tco}}{2}) - \frac{\Delta T k_{tco} k_l t}{\Delta h \rho_l} = 0$$

$$s(t) = L_{tco}(1 - \frac{k_l}{k_{tco}}) + \frac{1}{k_{tco}} \sqrt{\frac{k_l(\Delta h k_l \rho_l L_{tco}^2 + 2(T_0 - T_m)k_{tco}^2 t)}{\Delta h \rho_l}} \tag{3.13}$$

Lastly, to estimate the liquid fraction using the analytical expressions derived in equations 1.7 and 3.13, for the scenarios with and without TCOs, equation 3.14 was used. The PCM height, h_{pcm}, is equal to 5 cm in the experimental setup.

$$LF(t) = \begin{cases} \frac{s(t)}{h_{pcm}} & \text{, for melting tests} \\ 1 - \frac{s(t)}{h_{pcm}} & \text{, for solidification tests} \end{cases} \tag{3.14}$$

3.3.2 Numerical model

3.3.2.1 General description

Modeling the phase change process with the addition of TCOs in CFD enables capturing the temperature dependency of thermal properties and allows modeling scenarios in which the melting process is driven by convection. As described in Section 1.3.3.2, Ansys Fluent employs the enthalpy-porosity method to model phase change processes. For simplicity, and considering that the TCOs used in the experiment are cylinders occupying the entire z-direction and that heat transfer occurs mainly in one direction, the y-axis, the model could be simplified to a 1D case if we focus solely on the experiment. However, since the model is intended to be used to study additional hypothetical scenarios where heat is applied from the sides, it is defined as a 2D model in the xy-plane. The model domain is filled with OM29 and consists in a rectangular plane of 92 mm x 50 mm in length and height, as shown in Figure 3.11. The side walls are considered adiabatic. During the melting experiments, the top wall is taken as a constant temperature boundary ,T_{hot}, whereas the bottom boundary is considered to be adiabatic. The opposite occurs during the solidification experiments, where the top boundary is considered adiabatic and the bottom wall has a constant temperature, T_{cold}. Due to the viscous nature of PCMs, the flow is considered to be laminar.

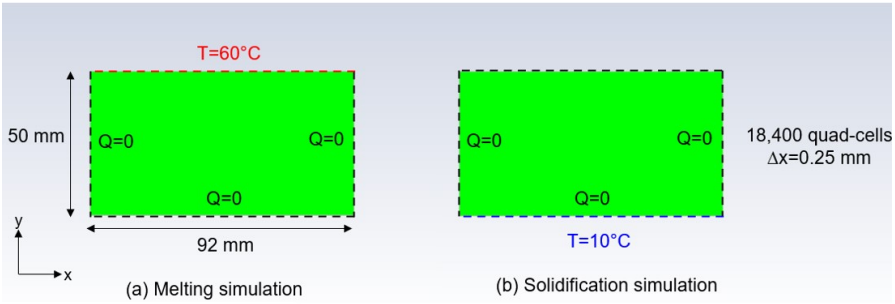

Figure 3.11: Model domain used in Fluent.

The numerical simulation was done using the coupled solver for the pressure-velocity coupling, the PRESTO! scheme for pressure discretization, the second order upwind scheme for momentum and energy and the second order implicit scheme for the transient formulation. The mesh was made of structured quad-cells and the time and cell size were defined from a cell size and time step independency analysis. Figure 3.12b shows the average liquid fraction and temperature evolution of the PCM during the melting test with T_{hot}=60^{o}C, considering Δx is equal to 0.5 mm and 0.25 mm, and Δt is fixed to 0.25 s. In Figure 3.12a instead, Δx is fixed to 0.25 mm and the results for Δt equal to 0.25 s and 0.5 s are compared. From these figures, it can be seen that results are similar, which allows us to conclude that results are already independent from the mesh and time step when Δx and Δt are equal to 0.25 mm and 0.25 s, respectively.

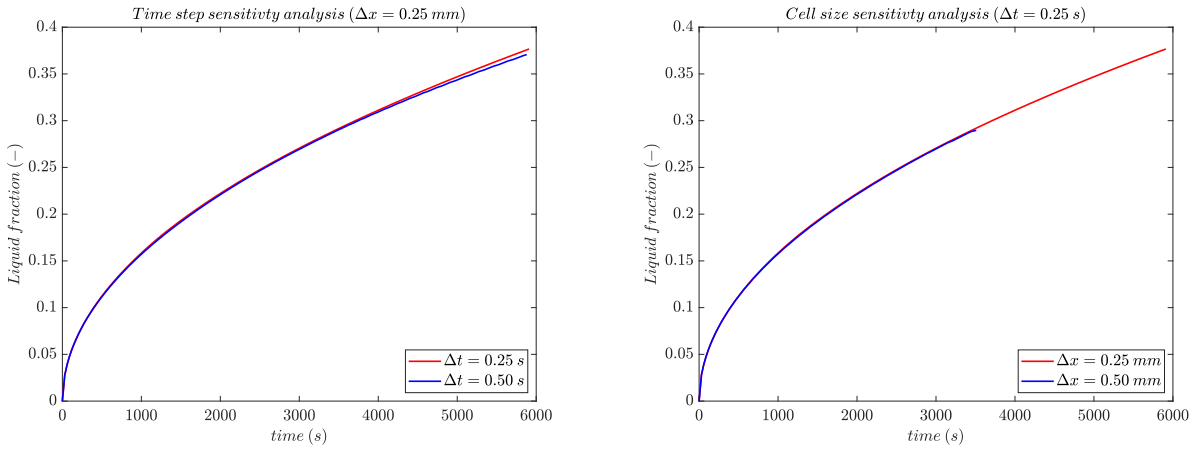

(a) Time step sensitivity analysis (Δx=0.25 mm).

(b) Cell size sensitivity analysis (Δt=0.25 s).

Figure 3.12: Liquid fraction evolution in Fluent, for different cell sizes and time steps.

3.3.2.2 Moving cylinders

To model the motion of a solid object along the solid-liquid interface, an initial approach involved using a dynamic mesh in conjunction with the six degrees of freedom (6DOF) method. However, achieving a stable solution for the motion of the solid object required a time step of 1e-04 seconds. This requirement significantly extended the simulation duration, making it impractical given that the melting time of the experiment was on the order of hours. A different approach was used instead to locally modify the thermal conductivity of the PCM at the solid-liquid interface, by using a user-defined function (UDF). This UDF used two Fluent predefined macros. The first one was DEFINE_EXECUTE_AT_END, a general purpose macro executed at the end of each time step, which is used to find the y-coordinate of the bottom of the TCO, y_{int}. Initially, when the PCM is completely solid, the TCOs are placed at the top of the PCM, as shown previously in Figures 2.1a and 2.1b, and therefore y_{int} is equal to PCM enclosure height, h_{PCM}, minus the height of the TCO, h_{tco}. However, as time proceeds and liquid forms beneath the TCO, y_{int} follows the solid-liquid interface. To detect the y-coordinate of the solid-liquid interface, the UDF makes a loop through all the cells in the domain, get the cell's liquid fraction $LF(i)$, and gets the maximum y-coordinate among the cells which have a liquid fraction below 1, as described in the scheme below.

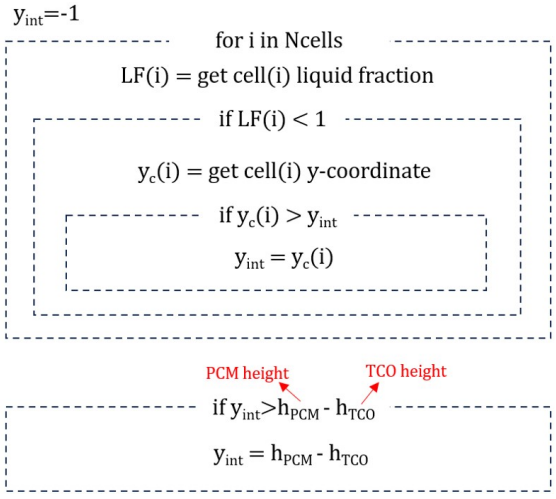

Figure 3.13: Scheme of the user-defined-function used to find the y-coordinate of the bottom of the TCO.

The second macro was DEFINE_PROPERTY, which was used to specify the thermal conductivity of the PCM as a function of temperature and the y-coordinate of each cell, y_c, according to Figure 3.14. If the cell y-coordinate is within the y_{int}, previously found in DEFINE_EXECUTE_AT_END, and the TCO's height, h_{tco}, the thermal conductivity will be equal to the effective thermal conductivity of the TCO, K_{tco}. If this is not the case, then the thermal conductivity assumes a piecewise-linear relation that varies between the thermal conductivity of the solid and liquid PCM. Details about the code used for each UDF can be

found in the Appendix B.

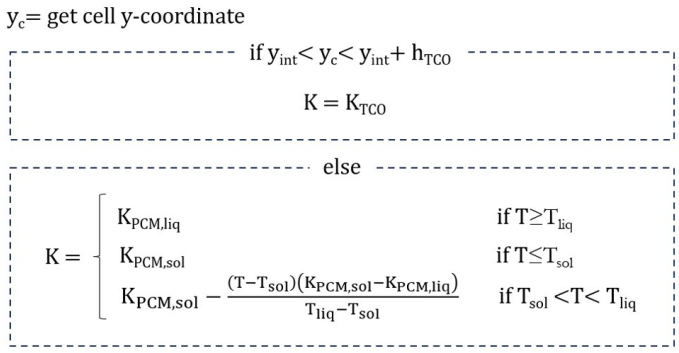

Figure 3.14: Scheme of the user-defined-function used to define the thermal conductivity of the PCM.

Chapter 4

Experimental results

4.1 Melting and solidification without cylinders

This section present the melting and solidification tests when no cylinders are added to the PCM. These results are used to validate the numerical model and see whether the thermal properties of the PCM and the assumptions made on the boundary conditions of the model are valid. The mass of the PCM for each experiment was determined at the start by subtracting the mass of the empty box from the mass of the box containing the PCM, resulting in 413 g and 420 g of PCM for the melting and solidification tests, respectively.

4.1.1 Experiment 1: Melting without cylinders

The first experiment, was done following the preheating and heating procedures described earlier and shown in Figures 3.8a and 3.8b, respectively. During the experiment, the following deviations from the original plan occurred. In the preheating phase, the PCM was heated up to 23.5-24.5^{o}C instead of 25^{o}C. The reason for this was that the hot thermal bath had a tendency to increase its temperature above the setpoint and there was a risk of starting the melting of the PCM prematurely. Therefore, to prevent this from happening, the heating phase began at a lower temperature from what was planned. In the melting phase, the hot thermal bath was set to 60^{o}C. However, since the hydraulic circuit and the heat exchanger were at ambient temperature, it took 4 minutes and 31 seconds for the water at the heat exchager inlet to reach 59^{o}C, as shown in Figure 4.7. For being able to compare the experimental results with the model, the time in which the temperature inlet reached 59^{o}C was defined as the zero reference for time.

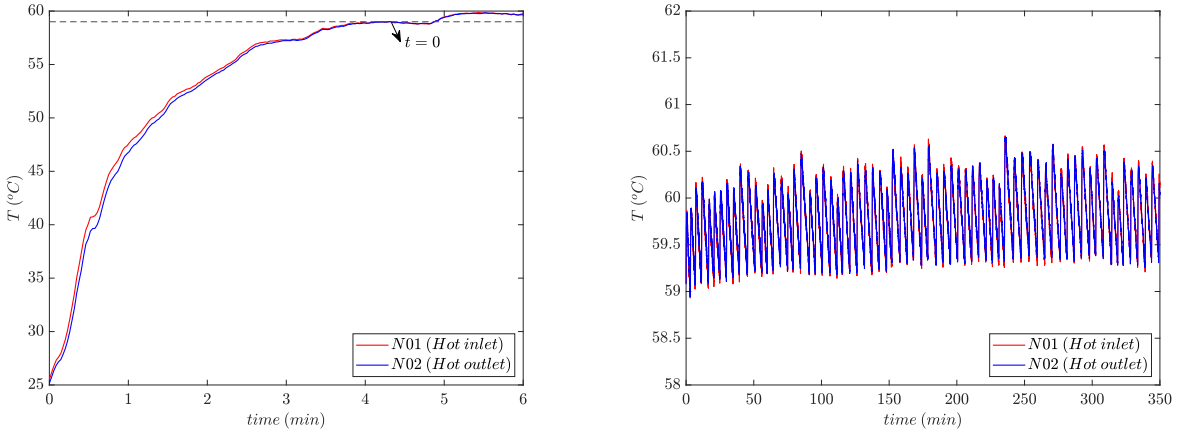

(a) Zoomed in at the starting time.

(b) General overview.

Figure 4.1: Inlet and outlet water temperatures of the heating plate.

The melting experiment was run for approximately 6 hours. During this time, the maximum and minimum inlet temperatures at the hot plate were 60.67^{o}C and 58.93^{o}C, respectively. The average temperature for the inlet and outlet of the hot plate was 59.77^{o}C and 59.78^{o}C, respectively, which means the temperature throughout the top plate was relatively constant. On the other hand, the bottom cold plate had a tendency

to increase its temperature because of heat conduction through the pipes. To prevent this from happening, water was circulated at 24^{o}C in the bottom plate, which was close to the initial temperature the PCM had.

Figure 4.2 shows the melting sequence of the PCM, with pictures every 30 minutes, approximately. The impurities observed in these pictures correspond to the thermal epoxy, which reacted with the fatty acids of the paraffin as it got heated. Each picture was processed in Matlab, to obtain the liquid (red) and solid (blue) regions. Then, based on the fraction of the liquid area with respect to the total area of the picture, the liquid fraction was estimated.

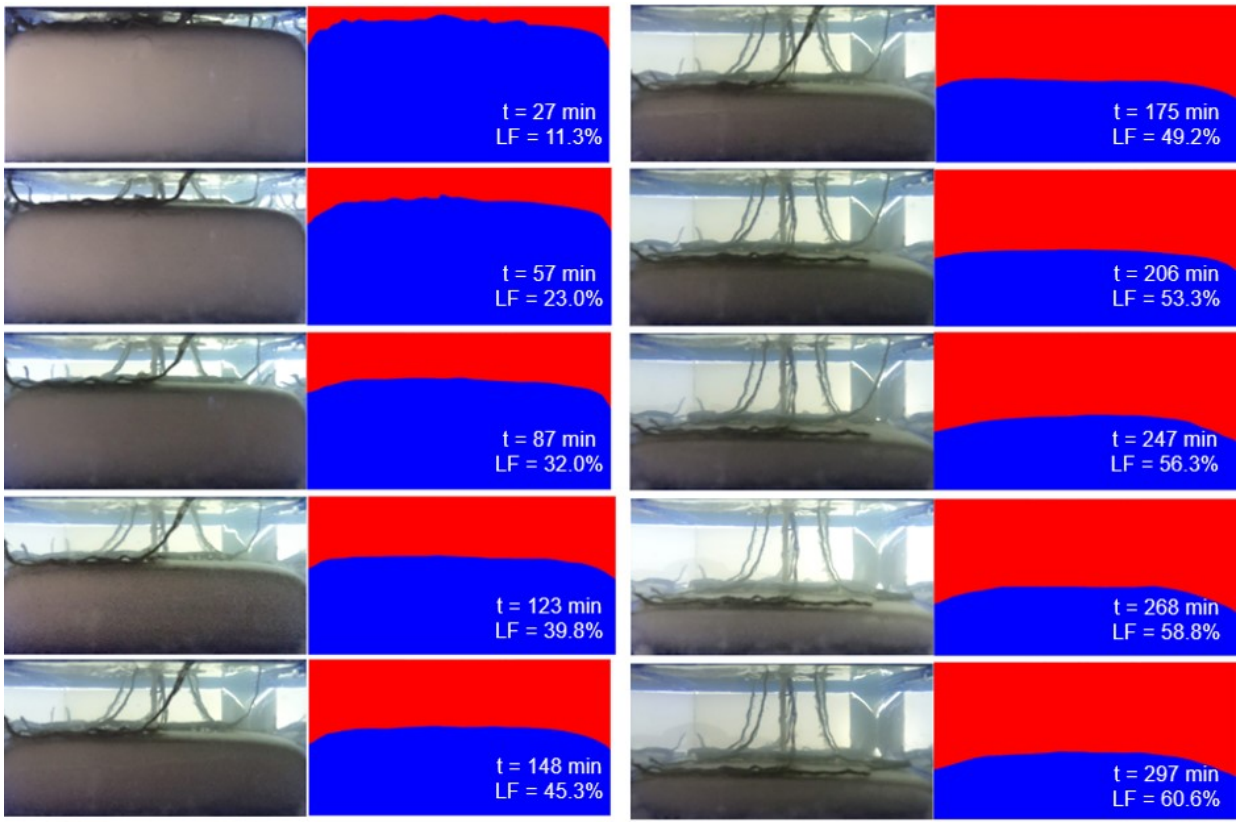

Figure 4.2: Liquid fraction evolution during the melting of the PCM without the addition of cylinders.

Figure 4.3a shows a comparison of the liquid fraction evolution between the experiment, the analytical model and the numerical model in Fluent. The different curves show a good agreement, though the models tend to overestimate the liquid fraction. This discrepancy can be primarily attributed to heat transfer through the lateral walls of the experiment, which is not accounted for in either of the models. This is evident from the curved shape of the solid-liquid interface near the walls, a phenomenon typically observed when a PCM is heated laterally. Initially, a thin, vertical layer of liquid PCM forms adjacent to the walls. Due to unstable thermal stratification, warmer liquid PCM rises, inducing a convective flow that shapes the edges of the solid PCM. Consequently, as some heat is lost through the walls, less heat is available to melt the solid PCM, resulting in a slower melting process in practice. A more significant discrepancy between the modeled and experimental liquid fractions is observed at the beginning of the plot, particularly between 0 and 50 minutes. This can be attributed to air gaps between the heating plate and the top surface of the solid PCM at the start, which introduce additional thermal resistance and reduce the heat transfer rate. Although the plexiglass enclosure was completely filled with liquid PCM as per the procedure described in 3.2.3, PCM contraction during solidification, which can range from 8-12% for paraffins [67], likely led to the formation of these gaps. As the experiment progressed and liquid PCM formed at the top, these air gaps disappeared. It is also important to note that when observing the liquid fraction from a single plane, the wall effects of the front and back walls are not visible. This implies that the experimental liquid fraction might be slightly underestimated by the pictures, as the solid PCM is expected to curve downwards as it approaches these walls. If we observe the comparison of the experimental and modeled temperatures shown in Figure 4.3b, we see that the simulation in Fluent tends to overestimate the experimental temperatures, which similarly as with the liquid fraction plot, can be explained by the fact that there was most likely an air gap between the solid PCM and the top heat exchanger in the beginning of the experiment.

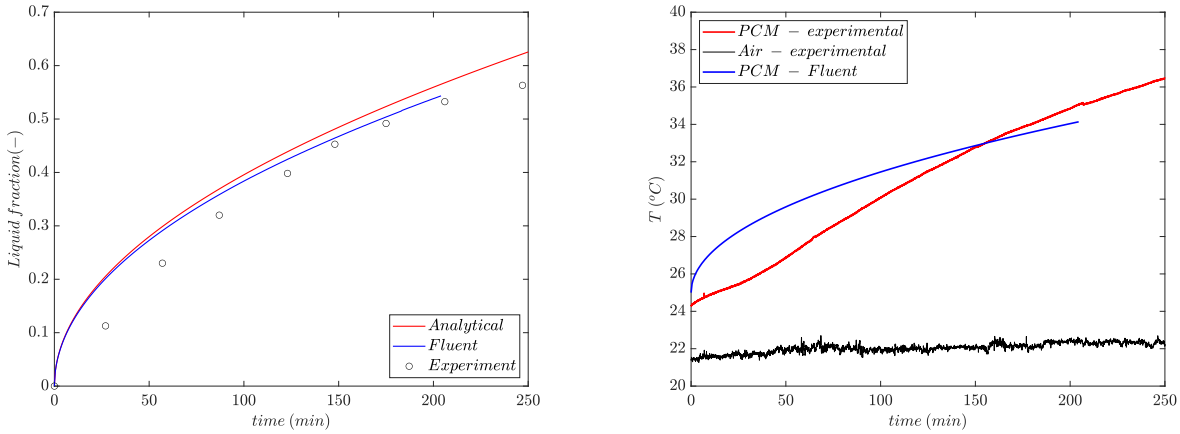

(a) Liquid fraction evolution.

(b) Average PCM and air temperatures.

Figure 4.3: Comparison between experimental and modeled results in the melting test without cylinders.

Figure 4.4 shows the temperature evolution of the PCM at five different heights, as shown earlier in Figure 3.5. The distance for each thermocouple is measured from the top heating plate. From the different curves, we observe that above the liquidus temperature, which is 28^{o}C, the slope of the curves increases. This behavior is explained by the fact that after the liquid phase is reached, heat is transferred as sensible heat only. However, as the liquid PCM gets hotter, the temperature difference between the heating wall, $T_{hot} = 60^oC$, and the PCM decreases, leading to reduced heat transfer and a subsequent decrease in the slope of the curve over time. When the PCM reaches the solidus temperature instead, which is 25^{o}C, heat is transferred as latent heat, and the temperature is expected to remain constant until the phase transition occurs.

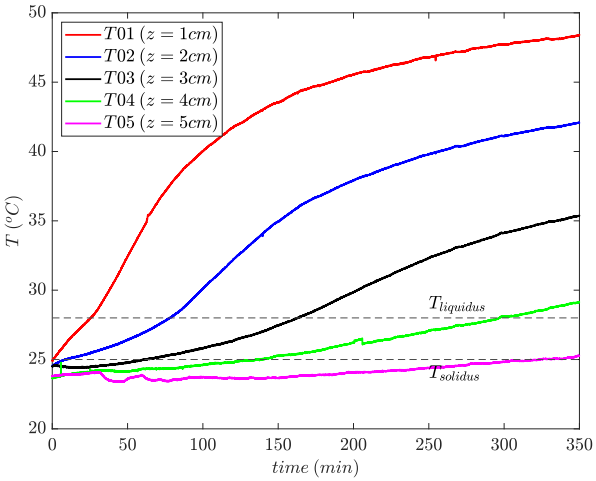

Figure 4.4: PCM temperature at different heights during the melting test without cylinders.

4.1.2 Experiment 2: Solidification without cylinders

In the solidification experiment, similarly to the previous experiment, the preheating and cooling procedures were followed according to Figures 3.8a and 3.8c, respectively. After the liquid PCM was preheated to approximately 30^{o}C, water at 10^{o}C was run through the bottom heat exchanger. To prevent the top heat exchanger from getting cooled through conduction, water at 30^{o}C was recirculated in the top heat excharger during this test. After the cold thermal bath reached 10^{o}C and the valve for water to circulate in the bottom heat exchanger was open, it took 6 minutes and 4 seconds for the water to go from 30^{o}C to a temperature below 11^{o}C, as shown in Figure 4.5a. To compare experimental results with the simulations, the zero reference for time was defined by the moment in which the water temperature at the inlet was below 11^{o}C. The solidification experiment was run for approximately 3 hours and 30 minutes. During this time, the standard deviation of the water temperature at the inlet and outlet was 0.05^{o}C and 0.06^{o}C, respectively. The average temperatures instead, for the inlet and outlet, were 10.35^{o}C and 10.43^{o}C, respectively.

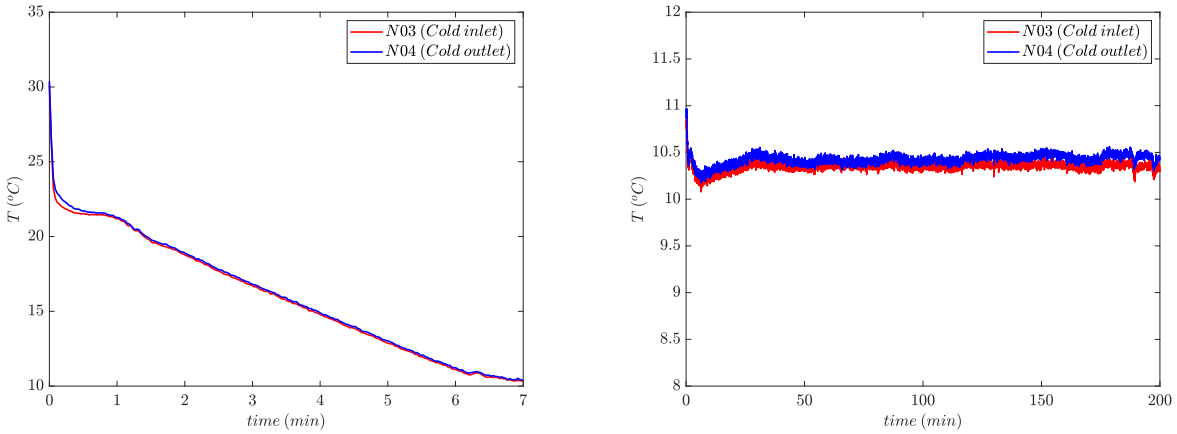

(a) Zoomed in at the starting time.

(b) General overview.

Figure 4.5: Inlet and outlet water temperatures of the cooling plate.

Figure 4.6 shows the liquid fraction evolution for the solidification process of the PCM without cylinders. Contrary to the melting experiment, when we observe the solidification process from the outer side of a wall, it is not possible to see the actual height of the solid region in the mid-section, leading to an overestimation of the solid fraction. This occurs because the solid-liquid interface bends upwards as it approaches the walls during solidification. As [68] explains it, when the solid forms, heat can be dissipated either in the axial direction through the solid PCM, or in the radial direction through the walls. Since the latter path offers a lower thermal resistance, solidification occurs at a faster rate near the walls, forming a basin-like structure.

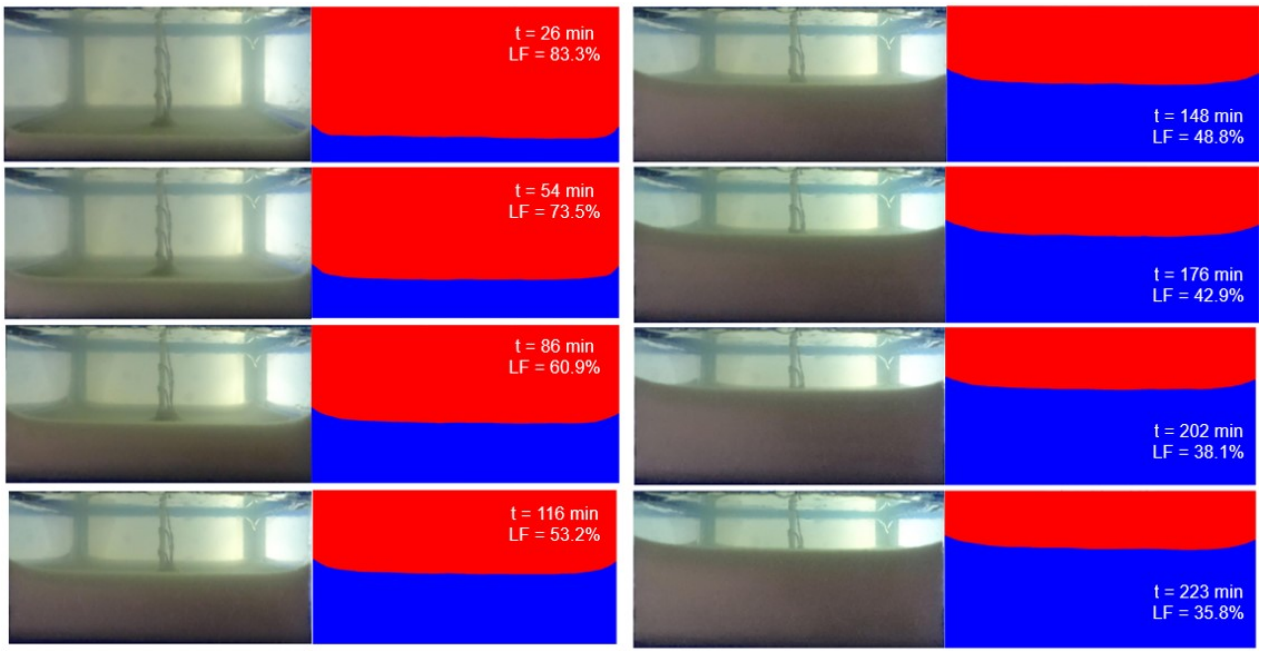

Figure 4.6: Liquid fraction evolution during the solidification of the PCM without cylinders.

Figure 4.7a shows a comparison of the liquid fraction evolution in the solidification test between the experiment, the analytical model and the numerical model. A good agreement is observed in the first 50 minutes. However as the experiment proceeds, the discrepancy between the modeled liquid fraction and the one observed in the pictures, increases, as the liquid fraction seen from the wall is underestimated. A better comparison between the modeled and experimental results can be obtained by comparing the temperatures. Figure 4.7b shows a comparison between the average temperature of the experiment and the numerical model. A similar trend is observed in both curves, with an offset which varies between 0.3 and 0.9°C. Some of the reasons which explain the fact that experimental temperatures are consistently lower than the modeled temperatures, is due to the heat losses to the side walls which are not accounted in the model.

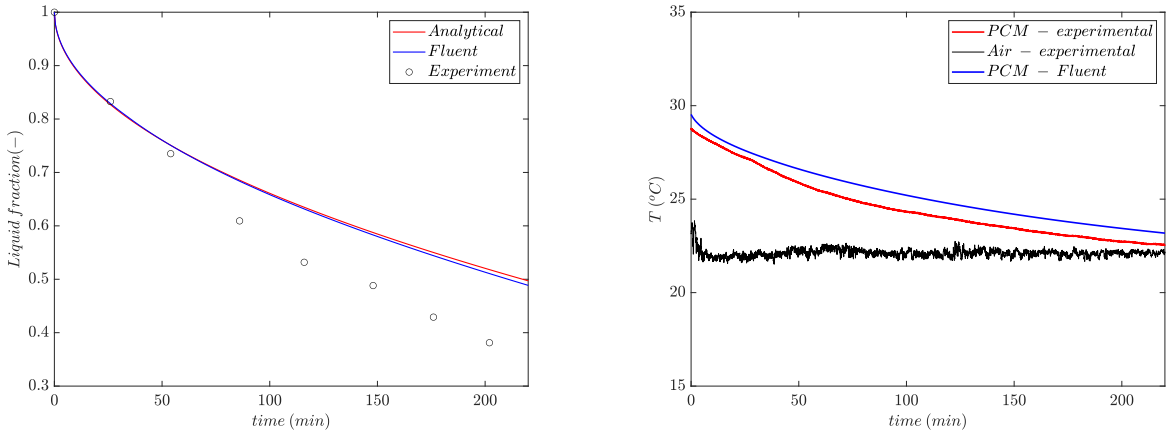

(a) Liquid fraction evolution.

(b) Average PCM and air temperatures.

Figure 4.7: Comparison between experimental and modeled results in the solidification test without cylinders.

Figure 4.8 shows the experimental temperatures of the PCM at five different heights, with z indicating the distance from the cooling plate. We can see from the different curves the change in their slope approximately at 25 and 28^{o}C, corresponding to the solidus and liquidus temperatures of the PCM.

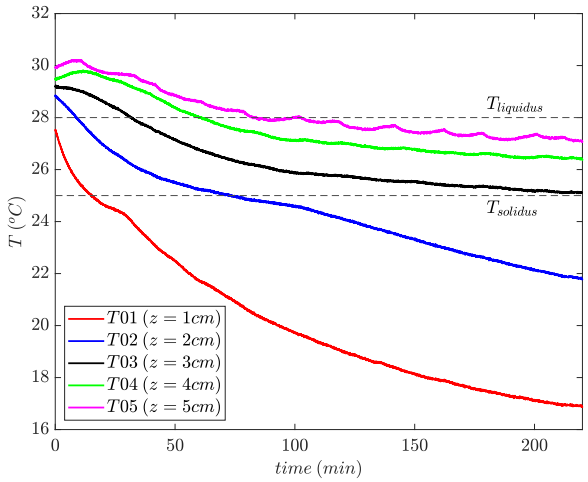

Figure 4.8: PCM temperatures evolution at different heights.

4.2 Melting and solidification with cylinders

In this section, melting and solidification tests were repeated under similar conditions, with the addition of 16 hollow aluminum cylinders. The objective of the melting test was to evaluate the improvement in the melting rate, while the solidification test aimed to observe whether the cylinders move together with the solid-liquid interface as the PCM solidifies. The experimental results for the melting test will be compared with the analytical solution of the modified Stefan problem and the Fluent model, which uses the developed UDF to modify the thermal conductivity of the PCM at the solid-liquid interface. The weight of the each cylinder varied between 1.52 to 1.58 g, with a total mass of 24.7 g. The mass of the PCM was determined by subtracting the mass of the cylinders and the empty box from the mass containing the PCM, resulting in 384 g for the melting test.

4.2.1 Experiment 3: Melting with cylinders

Similarly as with the previous melting experiment, the temperature setpoint for the top and bottom heat exchangers were 60^{o}C and 24^{o}C. After the hot thermal bath reached 60^{o}C and water was recirculated through the heating plate, it took 4 minutes and 17 seconds for the inlet water to have a temperature above 59^{o}C, as shown in Figure 4.9, and it was defined as the zero reference for time. The experiment was run

for approximately 3 hours and 30 minutes and during this time, the average temperatures for the inlet and outlet of the hot heat exchanger was 59.68 and 59.66 ^{o}C, respectively.

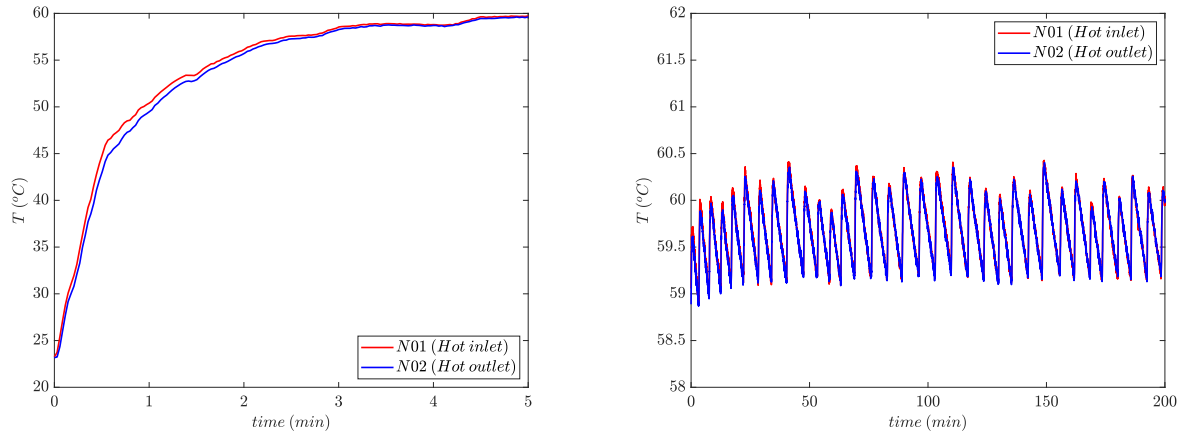

(a) Zoomed in at the starting time.

(b) General overview.

Figure 4.9: Inlet and outlet water temperatures of the heating plate during the melting experiment with cylinders.

Figure 4.10 shows the liquid fraction evolution of this experiment throughout time. It is important to note that adding cylinders introduces greater uncertainty in estimating the liquid fraction from a single plane image at the wall. Some cylinders are not perfectly horizontal and tend to incline toward the front or the back wall. This inclination can be attributed to an imbalance in their weight. Due to the higher thermal conductivity of the cylinders compared to the PCM, the solid PCM in contact with the cylinders tends to melt ealier. Consequently, if a cylinder tilts toward the front, the front part will melt at a faster rate than the PCM at the back, leading to an overestimation of the liquid fraction. Another observation from this sequence of images is that, even though the midsection of the PCM was not filled with cylinders, the height of the solid PCM in this region over time was relatively similar to that at the sides. This can be explained by the fact that if there is warmer liquid PCM on both sides of a colder solid PCM, the convective heat flux caused by the rising liquid PCM will accelerate the melting of the solid portion.

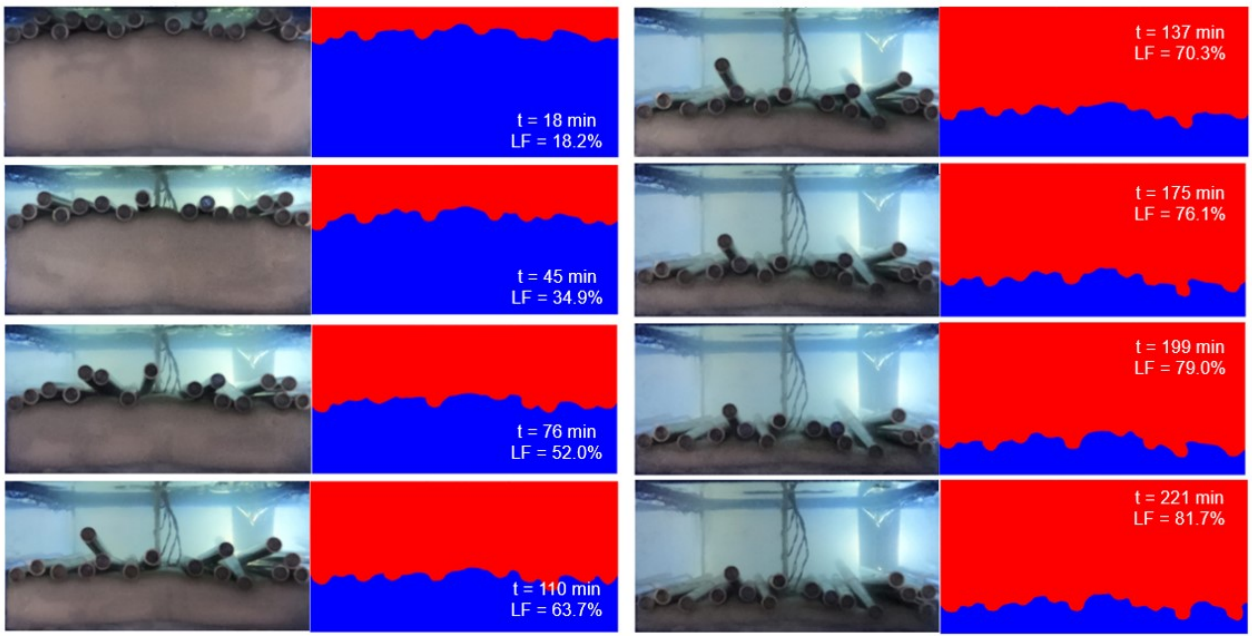

Figure 4.10: Liquid fraction evolution during the melting of the PCM with the addition of cylinders.

If we compare the experimental liquid fraction with the analytical and numerical models, we see that the models results give a lower liquid fraction, as shown in Figure 4.11a. This discrepancy may be due to

inaccuracies in estimating the liquid fraction from planar images of a wall. Additionally, when the cylinders tilt to one side, they increase the melting rate. Since the liquid PCM is thermally stratified, with warmer PCM at the top, a cylinder positioned higher on one side will conduct more heat than a horizontal cylinder, due to the greater temperature difference across the inclined cylinder. Figure 4.11b shows a comparison of the average temperature of the PCM between the experiment and Fluent. Similarly to the case without cylinders, we see an important discrepancy in the beginning (t<50 minutes), which can be given by the air gap that was initially between the solid PCM and the heating plate.

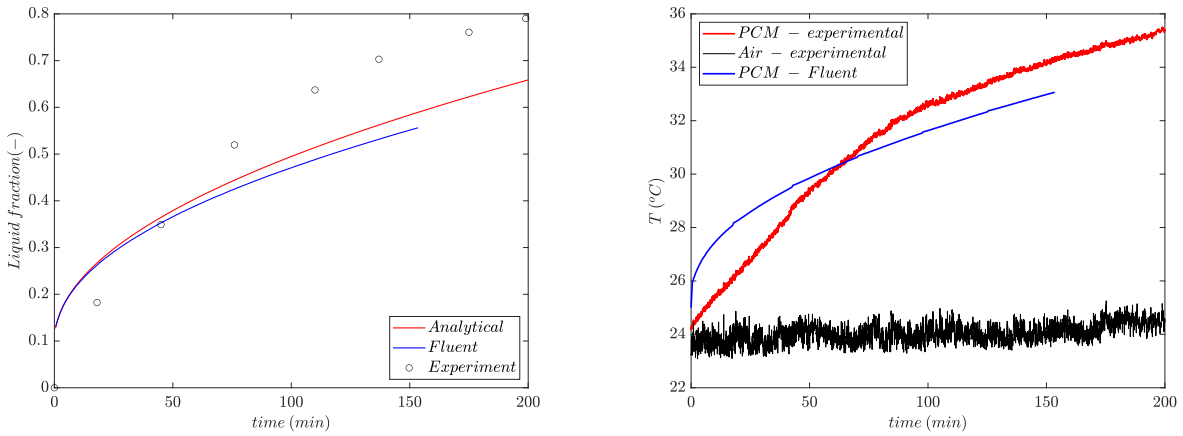

(a) Liquid fraction evolution.

(b) Average PCM and air temperatures.

Figure 4.11: Comparison between experimental and modeled results in the melting test with cylinders.

Figure 4.12 shows the PCM temperatures at different heights, with the distance z measured from the heating plate. We can see the curves follow a similar pattern to the one shown in the case without cylinders, but with the difference that the temperature increase occurs faster in this case. If we examine the intersection of the different curves with the melting temperature ($T_{liquidus}$), we can estimate the position of the solid-liquid interface. When no cylinders are added, this intersection occurs for T01, T02, T03, and T04 at 26, 78, 163, and 297 minutes, respectively. However, when the cylinders are added, the intersections occur at 10, 42, 79, and 156 minutes, respectively, clearly indicating an enhancement in the melting rate.

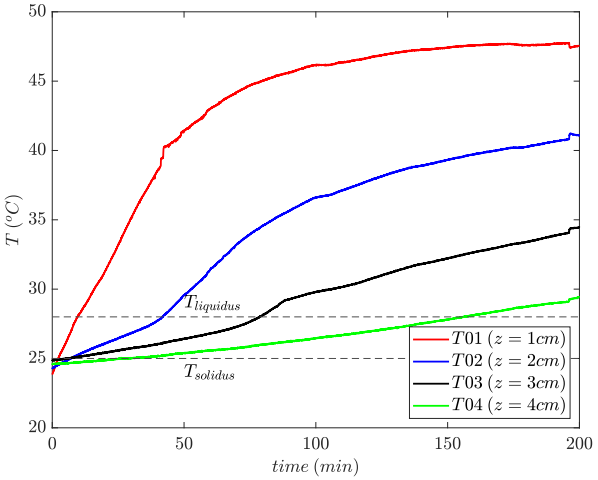

Figure 4.12: PCM temperatures evolution at different heights.

4.2.2 Experiment 4: Solidification with cylinders

The solidification test with cylinders was initially run under similar conditions as the case without cylinders. The cylinders were added before pouring the PCM, at the bottom of the plexiglass enclosure. The initial temperature for the PCM was approximately 30^{o}C and water was recirculated at 10^{o}C and 30^{o}C through the bottom and top heat exchangers, respectively. However, under these conditions, the cylinders

did not move with the solid front and were engulfed at the bottom of the PCM. Since the cylinders are denser than the liquid PCM, they can only float and be pushed upwards if they are within a denser and sufficiently thick mushy zone, so that buoyancy of the displaced volume is bigger than the weight of the cylinder. According to [64], when a fully liquid PCM is cooled from one wall, the mushy zone thickness is initially zero and increases with time as the solid front moves. Based on this observation, this test was repeated, but the cylinders were added instead when the solid front was already 1.5 cm and 3.0 cm above the cooling plate, as shown in Figure 4.13a. To see whether the wall-effect had an influence in the engulfment of the cylinders, one half of the enclosure was filled with 90-mm long cylinders, whereas the other half, was filled with 45-mm long cylinders, as shown in Figure 4.13b. However, in neither of the cases the particles were displaced and remained engulfed as the solid front moved upwards. The solidification of the PCM started throughout all the cylinder surface and therefore, the solid-liquid interface curved upwards as it went over the cylinders.

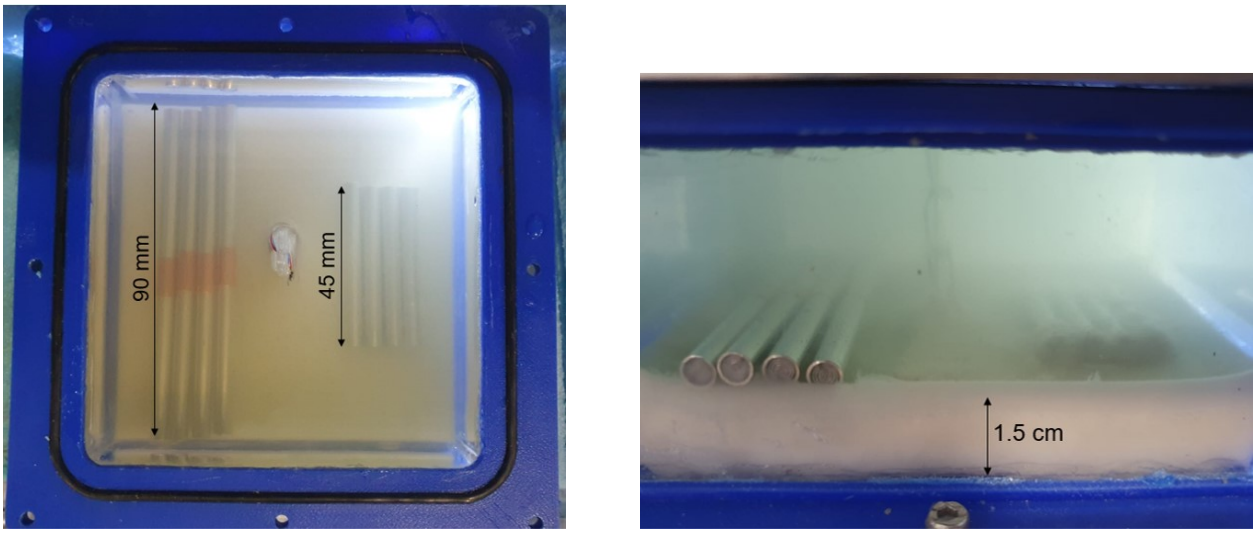

(a) Top view of the plexiglass enclosure.

(b) Side view of the plexiglass enclosure.

Figure 4.13: Addition of cylinders in the PCM after the solid front is 1.5 cm above the bottom.

Chapter 5

Discussion

5.1 Solid-liquid interface with and without cylinders

It is important to note the differences in the layer containing the TCOs between the experiment, the analytical model and the numerical model in Fluent, as illustrated in the scheme of Figure 5.1. In the first case, the analytical model takes the TCO as a distinct material from the PCM. As a result, the solid-liquid interface begins below the cylinders at t=0. In the second case, Fluent considers the TCO as part of the PCM, which is initially solid. Therefore, before the solid-liquid interface moves below the TCO, a certain amount of heat, equal to the latent heat of the PCM, must be absorbed. The thermal energy, E, required to melt 5 mm of OM29, can be calculated as the product of the mass of the PCM and its latent heat of fusion, according to equation 5.1, yielding 8013 J. Given the thermal conductivity of the layer of solid PCM with TCOs, which is 20.22 $W/m \cdot K$, the heat flux across this layer is 1198 W. Consequently, melting the initial layer takes 6.6 seconds.

$$E = m_{pcm,s}\Delta h = \rho_{pcm,s} V \Delta h \tag{5.1}$$

In the third case, the experiment places the cylinders within the PCM. Considering that 16 cylinders are embedded in the PCM, each with a length of 90 mm and an outer diameter of 5 mm, the first 5-mm layer consists of 33% PCM and 67% hollow aluminum cylinders. Using a similar procedure as with the Fluent model, melting the fraction of PCM within this layer requires 2671 J and takes 2.2 seconds. Since melting the complete PCM occurs within hours, we can consider this time difference between the experiment and the models to be negligible if we intend to compare the solid-liquid interface position throughout time. If we now use the analytical model to study the energy stored in the PCM throughout time, it is important to consider the energy stored in melting the first 5-mm layer in the case where the cylinders are added.

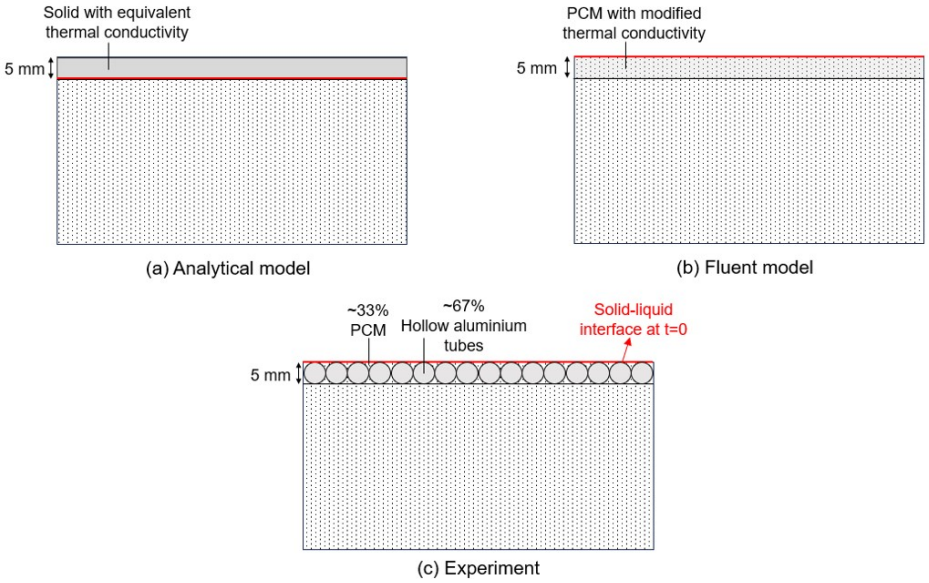

Figure 5.1: Solid-liquid interface position at the starting time for the analyical model, the Fluent model and the experiment.

Based on the analytical model, when a 5-mm layer with a similar effective thermal conductivity as the

cylinders embedded in the PCM is added on top of the PCM, the solid-liquid interface position is consistently 5 mm lower than the case with only PCM. This results in the complete PCM melting in approximately 19% less time, as shown in Figure 5.2a. In terms of thermal energy stored, the PCM is able to store approximately 71 kJ after its fully melted, whereas in the case without cylinders this value reduces to 67 kJ, as shown in Figure 5.2b. This decrease in the thermal energy stored is explained as part of the PCM volume is replaced by the cylinders. On the other hand if we look at the thermal power in Figure 5.2c, we only observe a significant increase of the heat flux with the addition of cylinders in the beginning. For example, if we consider the first 10 seconds, the stored thermal energy, given by the area below the curve, is 218% higher in the case with cylinders with respect to the case without cylinder, increasing from 1127 J to 3591 J. However this difference rapidly decreases as the liquid PCM between the heat source and the layer with the cylinders increases in thickness and its thermal resistance becomes dominant. After 110 seconds, the heat flux in the case with cylinders is only 1% bigger than the case without cylinders. We can analyze this result by looking at the thermal resistances between the solid-liquid interface and the heat source by using equation 3.11. We can see from Figure 5.2d that the thermal resistance of the 5-mm layer with the TCOs, R_{tco} is constant in time, whereas the thermal resistance of the liquid PCM, R_{PCM} begins as zero, but as soon as liquid starts to form between the thermally conductive layer and the heat source, it increases rapidly and becomes the dominant thermal resistance.

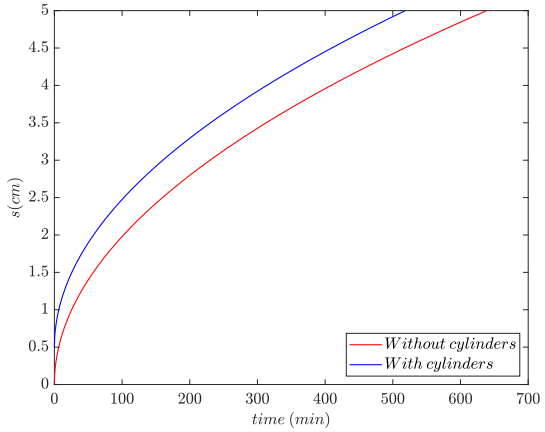

(a) Solid-liquid interface position.

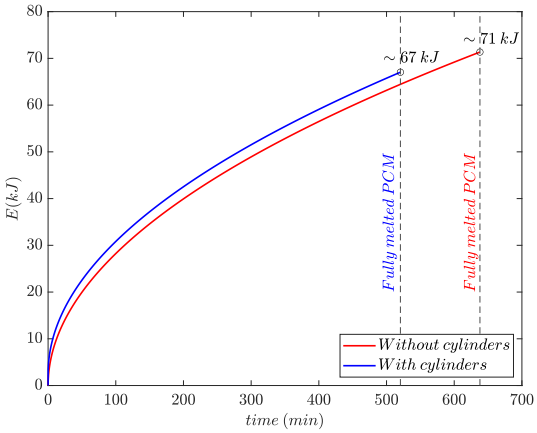

(b) Stored thermal energy in the PCM.

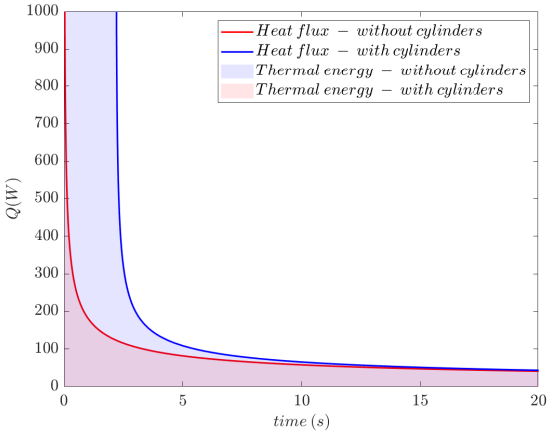

(c) Heat flux dissipation.

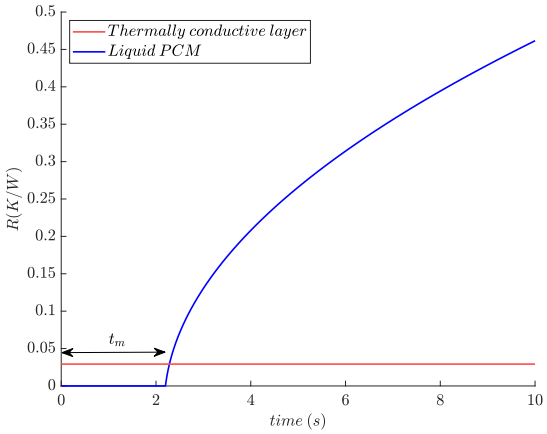

(d) Thermal resistances.

Figure 5.2: Melting process of the PCM with and without the addition of cylinders, when the top wall is heated at 60°C.

5.2 Melting rate and cylinder's physical properties

A straightforward method to study the effect of different physical properties of the cylinder on the melting time of the PCM is to use the analytical model presented earlier. The parameters of the cylinders affecting the melting rate are the cylinder's height and thermal conductivity. If we look at the analytical solution for the solid-liquid interface position of equation 3.13, when the time term t is big enough, the

cylinder's properties only affect significantly the first term:

$$s(t) \propto L_{tco}\left(1 - \frac{k_l}{k_{tco}}\right) \tag{5.2}$$

Figure 5.3a shows the melting front evolution for the current cylinder height of 5 mm (blue curve), and for a change in its height in +75% (black dotted curve) and -75% (red dotted curve), while keeping the rest of the parameters unchanged. The curve's behavior is explained by the direct relation between L_{tco} and $s(t)$ shown in equation 5.2, valid for t>>0. On the other hand, Figure 5.3b shows the melting front evolution for the current cylinder's layer effective thermal conductivity of 20.22 W/m·K (blue curve), and for two additional values, while keeping the rest of the parameters unchanged. The red-dotted curve represents the melting front when the thermal conductivity of the cylinder's layer is equal to the liquid PCM, 0.172 W/m·K. Based on the previous equation 5.2, there is an asymptotic relation between $s(t)$ and k_{tco}, because as k_{tco} increases, the value in the parenthesis approaches to 1. Therefore, we can expect the change in the melting front position to be negligible when k_{tco} increases above a certain value. In this example, we can see that when k_{tco} is equal to 4 W/m·K , the value in parenthesis is above 0.95, which is already close to 1, and therefore further increases in the thermal conductivity have a minor impact in the melting rate.

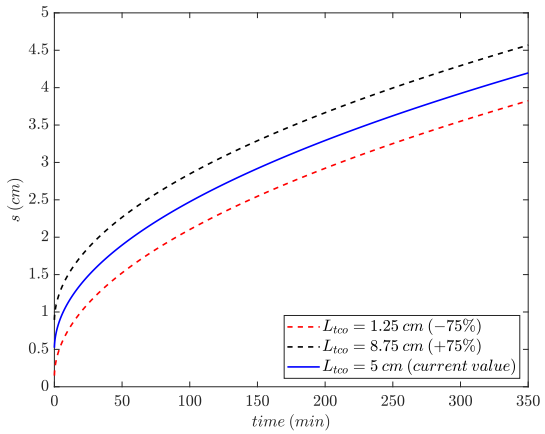

(a) Sensitivity analysis on the cylinder's height.

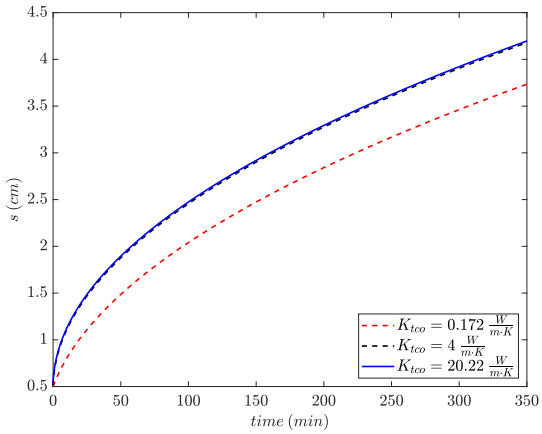

(b) Sensitivity analysis on the cylinder's effective thermal conductivity.

Figure 5.3: Melting front evolution as a function of the cylinder's height and thermal conductivity.

5.3 Convective driven melting - hypothetical cases

5.3.1 Convection with and without a thermally conductive layer

In a practical scenario where the goal is to maximize heat transfer into a latent heat storage unit, the melting of the PCM should be driven by convection. One approach to achieve this is by heating one side of the enclosure. For this analysis, the same PCM and enclosure will be used, but with the enclosure rotated 90° so that the heating wall is positioned on the left side, as shown in Figure 2.1a. However, instead of using small thermally conductive objects, a single thermally conductive layer will be employed, with its thermal conductivity being 20.22 $W/m \cdot K$, to maintain similar thermal properties as in the previous case. This layer will function as a moving fin as the melting front progresses downward. The decision to forgo smaller objects is based on the fact that PCM between them would create additional thermal resistance. In contrast, a single layer can maintain close contact with the heating wall, effectively acting as a moving fin. To model this layer, the UDF described in 3.3.2.2 was used. The height and width of the enclosure are 92 mm and 50 mm, respectively, the left side wall has a constant temperature of 60°C and the rest of the walls are adiabatic.

Figure 5.4 shows the melting sequence of the PCM when there is no thermally conductive layer. This case is used as a reference to assess the improvement in the melting rate when the thermally conductive layer is included. The dimensions and boundary conditions are the same, with the left wall maintained at a constant temperature of 60^{o}C. Initially (<10 min), the liquid PCM forms a relatively vertical layer as the melting process occurs more uniformly, which can be explained by the dominance of conductive heat transfer. As time progresses, convective heat transport becomes more significant in the melting process. This is evident from the curved shape of the solid-liquid interface, which results from the buoyant flow of warmer,

less dense PCM rising to the top of the enclosure. These flows significantly enhance the heat transfer to the solid PCM compared to the purely conductive melting case, reducing the melting time from 638 to 104 minutes. However, as described in other studies [12, 46], melting in bottom right corner remains a slower process, as the buoyant flow of warmer PCM does not effectively reach the bottom right side. In this case in particular, melting the last 25% of solid fraction takes 371% more time than melting the initial 25%.

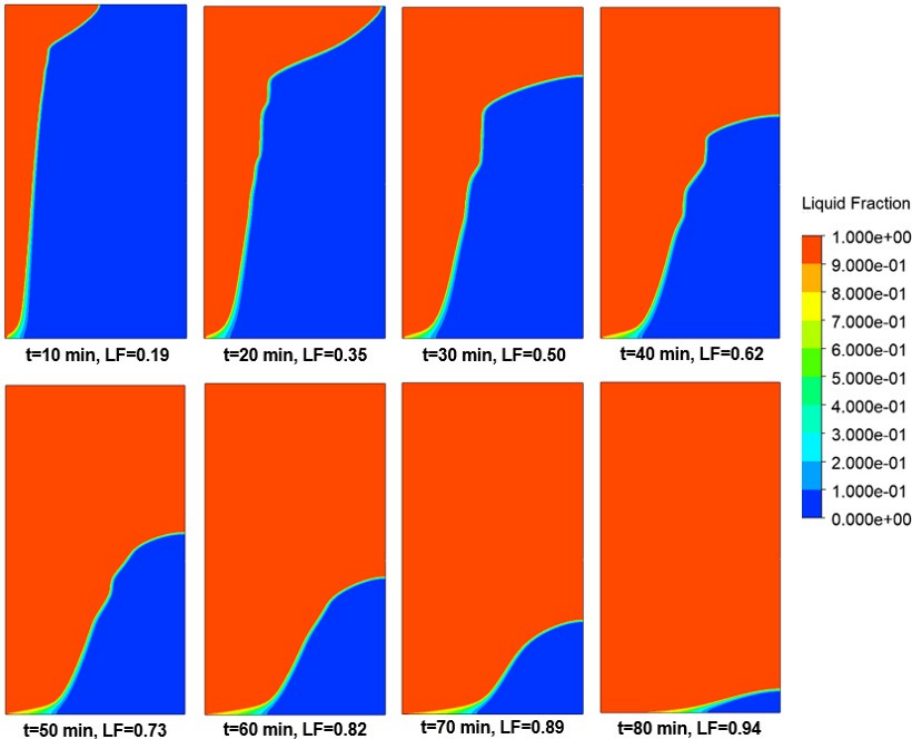

Figure 5.4: Liquid fraction evolution when the PCM without a TCO is heated from the left side.

If we now study the scenario with the inclusion of a thermally conductive object, in the form of a horizontal layer that moves with the solid-liquid interface, the melting time can be reduced even further to 39.5 minutes—62% lower than in the previous case. Figure 5.5 shows the melting sequence of the PCM with the addition of the thermally conductive layer. We can see from the beginning the faster penetration of heat at the top of the enclosure as the TCO offer a path with a lower thermal resistance than the solid PCM. Liquid PCM initially forms a relatively horizontal layer on the top (<10 minutes), but we also observe the formation of a vertical layer of liquid PCM on the left side, similar to the previous case. As time progresses (>15 minutes), the thermally conductive layer begins to move with the solid-liquid interface, eventually becoming completely flat at the top, which means that melting through conduction is the dominant heat transfer mechanism below the PCM. If we look at the temperature across the TCO at different time steps, we see it decreases as it moves away from the heating wall, meaning the melting of the layer of PCM below the TCO occurs from left to right. However, we still see a flat solid-liquid interface throughout time, which can be explained by the fact the thin layer of liquid PCM that forms on the left side of the solid-liquid interface dampens the melting rate as it adds an additional thermal resistance between the solid PCM and the TCO, whereas the right side of the TCO remains in close contact with the PCM. As a result, uniform melting occurs beneath it, driven by conduction. On the left side, the solid-liquid interface evolves similarly to the previous case, bending towards the top due to convection.

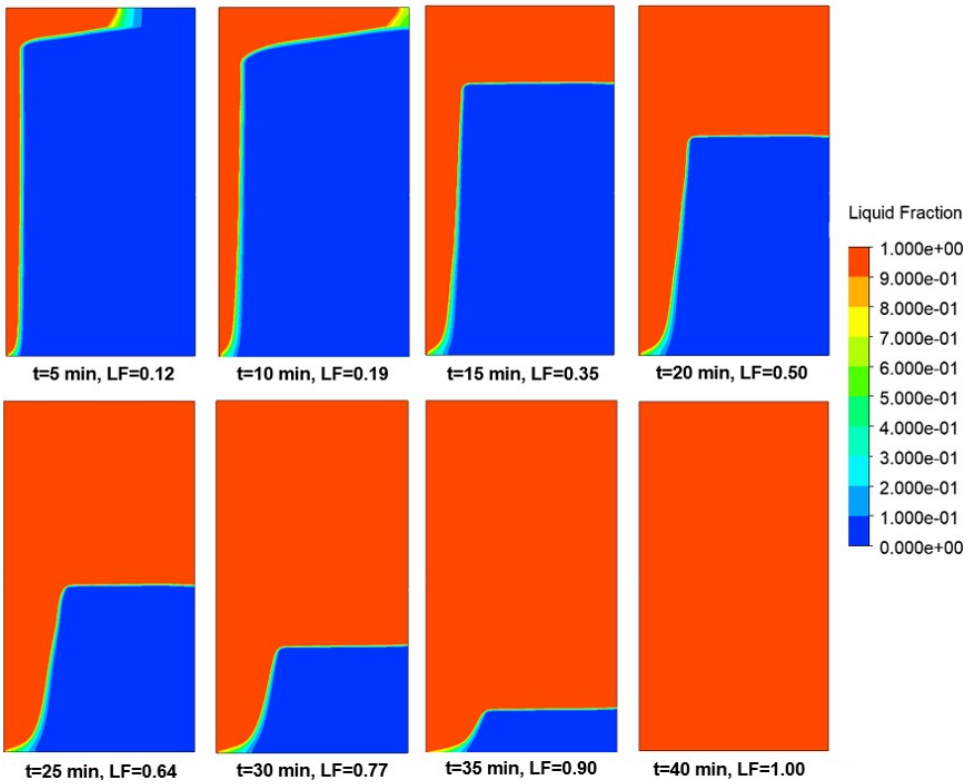

Figure 5.5: Liquid fraction evolution when the PCM with a TCO is heated from the left side.

Figure 5.6a shows a comparison of the liquid fraction evolution between the two convective melting cases. In the case without TCO, represented by the red curve, the liquid fraction increases linearly over time and decreases significantly during the final 10% of solid fraction, as conductive melting becomes dominant. Figure 5.6b presents a comparison of the area-weighted average heat flux through the left wall. The shape of the curve for the case without TCO highlights the three characteristic melting phases typically observed in PCMs heated from one side, as previously shown in Figure 1.6. During Phase I, conductive melting occurs with low thermal resistance, as the heat source is in close contact with the solid PCM. This results in a high heat flux that rapidly decreases as a vertical layer of liquid PCM begins to form. In Phase II, convective melting takes place, and the heat flux remains relatively constant with an average value of 26.5 W. Finally, in Phase III, the heat flux decreases as conduction once again becomes dominant.

In the case with TCO, represented by the blue curve, the liquid fraction begins to increase similarly to the case without TCO during the first 12 minutes. However, after this point, the melting rate increases considerably and progresses in a much more linear manner compared to the case without TCO. For example, if only focus on the region with a higher melting rate, we observe that melting 10% of the PCM takes 3.05 minutes when its moves from 30 to 40%, whereas it takes 3.75 minutes when it moves from 90 to 100%, which reflects a more consistent melting rate throughout time. If we look at the heat flux curve, we can see it is higher throughout all the melting process. It begins similarly to Phase I of the previous case, with a higher heat flux which rapidly decreases. However, its almost double in magnitude as the TCO allows heat to be transferred at a higher rate. Once the higher melting rate region begins (t>12 minutes), the heat flux increases up to 80 W and decreases in a relatively linear manner to 66 W, with an average value of 75.4 W. This increase in the heat flux occurs when the solid-liquid interface below the TCO becomes flat, maximizing the contact area between them. In this region, melting is driven by conduction on the top face and by convection of the left side, as a curved solid-liquid interface remains due to buoyant flows. The heat flux decreases over time as the solid-liquid interface at the top becomes narrows, reducing the contact area between the colder solid PCM and the TCO. During this phase of decreasing heat flux, small oscillations are also observed. These can be explained due to the fact that the solid-liquid interface flatness at the top is not perfect and changes over time. The peaks in the oscillations can be interpreted as moments in which the solid-liquid interface was flatter, resulting in a larger contact area between the solid PCM and TCO. On the other hand, the valleys in the oscillations, would represent the moments when the solid-liquid interface was less flat and tilted to the left, leading to a smaller contact area between the solid PCM and the TCO.

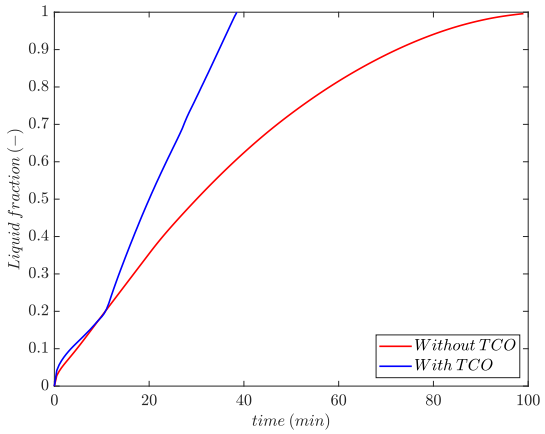

(a) Liquid fraction evolution of the PCM.

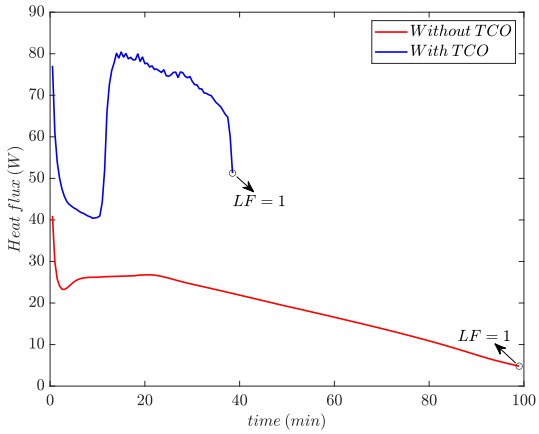

(b) Heat flux through the left wall.

Figure 5.6: PCM performance with and without the addition of a TCO when heated from the left wall ($T_{wall} = 60^oC$).

5.3.2 Thermal conductivity of the TCO

To understand the impact of the TCO's thermal conductivity on the melting rate of the PCM, two additional cases were modeled. The first case has a thermal conductivity ten times higher (K_{tco}=200 W/m K), and the second has a thermal conductivity ten times lower (K_{tco}=2 W/m K). All other parameters of the model remain the same, with the left wall maintained at a constant temperature of 60^{o}C. Figure 5.7 shows the liquid fraction evolution for these two cases, along with the previous case with K_{tco}=20 W/m K. In the case with higher thermal conductivity, represented by the blue curve, the high melting rate phase begins after approximately 8 minutes, which is 4 minutes earlier than in the original case, represented by the black curve. The complete melting occurring after 33 minutes, 5.5 minutes ahead of the original case. We can observe that the melting rate during the high melting rate phase is relatively similar and their offset is mainly given by the fact that this phase begins earlier in the case with higher thermal conductivity. On the other hand, when we look at the case with lower thermal conductivity, represented by the red curve, the melting rate decreases more considerably, taking 71 minutes to fully melt. As the TCO takes longer to melt the right side of the PCM, it gives more time for convection to melt the left side of the PCM, resulting in a smaller contact between the TCO and the solid PCM.

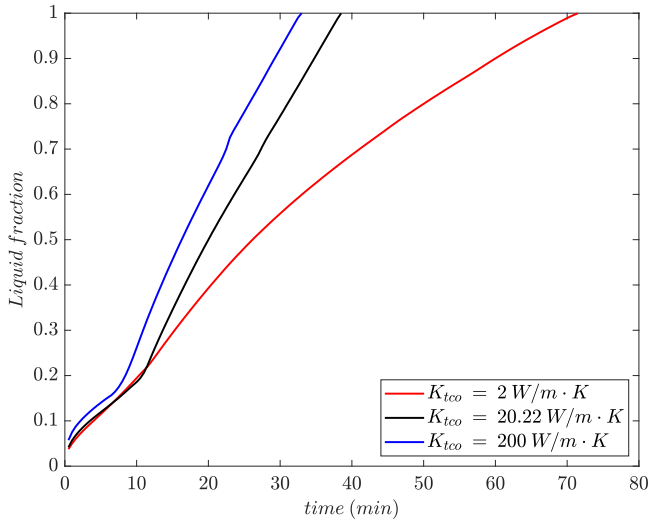

Figure 5.7: Sensitivity analysis of the thermal conductivity of the TCO under convective melting.

5.3.3 Model remarks

The main limitation of the developed UDF in Fluent, is the fact that the thermally conductive layer in reality is a solid, but is treated as part of the fluid in the model. In a purely conductive melting case this should not be a concern as heat transfer would be determined mainly by thermal conductivity. However, in a case where convection is relevant, the buoyant flows patterns should behave differently depending on whether this layer is solid or liquid. If the TCO was treated as a solid, as the region containing the TCO moves downwards, the liquid PCM beneath it should be more stagnant than what the model represents, as it would have a smaller distance to travel. As a result, the buoyant flow velocities are overestimated by Fluent, as it allows warmer liquid PCM to travel longer distances up to the top of the enclosure, as shown in Figure 5.8. This also means that the convective heat transfer coefficient at the left side of the solid-liquid interface is expected to be higher in Fluent than in reality. However, we can argue that this overestimation is relatively small; the solid-liquid interface evolves similarly in the cases with and without a TCO on the left side and the maximum velocities close to the solid-liquid interface are on the order of 0.007 m/s. On top of the flat solid-liquid interface, the liquid PCM is almost stagnant as we have a stable thermal stratification with warmer liquid PCM towards the top. This means the overestimation beneath the TCO should be even smaller and the higher melting rate can be attributed to conductive melting instead.

However, since there are no references in the literature on this modeling approach, it would be beneficial to validate it with an experimental setup. Additionally, future work should explore scenarios with different dimensions and thermal properties to better define the range of conditions in which the model is valid. For example, if the TCO's thermal conductivity is not sufficiently high, the overestimation of convective flows on the left side may become significant.

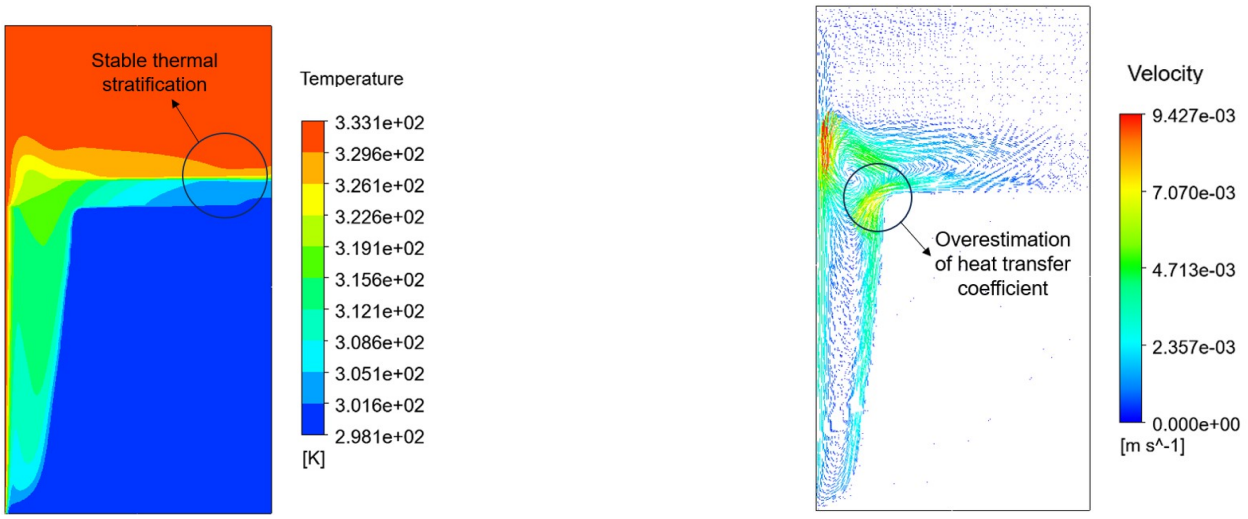

(a) Temperature contours in the PCM.

(b) Velocity vectors in the PCM.

Figure 5.8: Fluent results for the melting of the PCM with a TCO at t=20 minutes (K_{tco}=20.22 W/m K)

Chapter 6

Conclusions

This work explored the melting and solidification process of a PCM when a thermally conductive object (TCO) is added at its solid-liquid interface, with the goal of enhancing the melting rate and have a more uniform melting throughout time. The conclusions of this work are presented based on the specific research questions presented in the beginning.

(i) What is the optimum shape, size and material for the TCOs?

The optimum size for the TCOs was initially intended to be such that it could move with the solid front when the enclosure was cooled from the bottom. Additionally, the choice of hollow aluminum tubes as the TCO in the experiment was made primarily because it was an easily available material that matched the target density required to float on the mushy zone. Given that their density was similar to that of the mushy zone, their size was supposed to match the thickness of the mushy zone in order for them to float. Since this was not achieved in the experiment and the cylinders were engulfed at the bottom, the optimum size was not found for this purpose. If the focus shifts to improving the melting process when the enclosure is heated from the side instead, the optimum shape should ensure close contact with the heat source to maximize heat transfer to the solid, colder PCM. The sensitivity analysis on the thermal conductivity, showed that a thermal conductivity has to be such that melting through conduction below the TCO is faster than melting through convection on the side. In the examples shown in this work, beyond 20 W/m K, the PCM did not improve the melting rate significantly. On the other hand, when it was as low as 2 W/m K, the melting rate decreased more significantly because the left side of the PCM was exposed to convective melting for a longer time, causing the flat solid-liquid interface to become narrower and reducing the heat transfer between the solid PCM and the TCO.

(ii) How much will the melting rate improve?

The addition of TCOs under purely conductive melting with heating coming from the top decreased the melting time in 19% with respect to the case without TCOs. However, after the initial 12 mm of PCM were melted, the thermal resistance of the liquid PCM between the TCO and the heat source became dominant and the melting rate was almost the same as in the case without TCOs. When heating comes from the side wall instead and melting is driven by convection, results are more promising as the melting time decreased in 62% with respect to the case without TCOs. Additionally, considering the time in which the heat flux through side wall was relatively constant, the addition of TCOs increased the thermal power dissipation from 26.5W to 75.4W. Future research should focus on validating the model developed in Fluent, ideally through experimental setups, to ensure that it does not overestimate the heat transfer coefficient at the solid-liquid interface and to determine the range of cases in which it is applicable. Additionally, further analysis of the geometry and size of the TCO should be conducted to define them in terms of various operating conditions, rather than only for the specific case of the rectangular enclosure presented in this work.

(iii) Is the melting and solidification process repeatable?

Based on the solidification experiment with the addition of hollow-aluminium cylinders, it was not possible to move the cylinders with the solid front. Solidification started uniformly through the cylinder's surface, engulfing them within the solid PCM. Although it was not possible to confirm whether the cylinder dimensions were within the mushy zone thickness, the engulfment could be attributed not only to the lack

of sufficient denser mushy zone beneath them, but also to the fact that the solidifying PCM encountered a low thermal resistance path for releasing heat and initiating solidification on the cylinders, similar to what was observed on the walls. Irrespective of the reason, the only scenario in which the TCOs could potentially rise to the top is when cooling is applied at the bottom. However, this would only occur in the scenario involving conductive melting. In the scenario involving convective melting instead, one side wall is expected to be conductive, so if cooling was applied from the bottom, the side wall would potentially solidify as well, making it even more challenging to bring the TCOs to the top. Since the most promising results are for the case heated from one side, efforts should focus on developing a solution to make this scenario repeatable. A mechanical mechanism would be needed to bring the TCO back to the top of the enclosure each time the PCM is fully melted. Future research should evaluate different alternatives for this mechanism and balance the energetic benefits of a higher melting rate with the additional energy costs of moving the TCO after each cycle and the increased manufacturing costs the latent heat storage system would require.

Bibliography

[1] Niklas Schoch Francys Pinto Miranda Carlos David Yáñez de León Eren Çam, Zoe Hungerford. Electricity 2024, analysis and forecast to 2026. Technical report, International Energy Agency, 2024.

[2] Trevor Criswell Piotr Bojek François Briens Jeremy Moorhouse Yasmina Abdelilah, Heymi Bahar and Laura Mari Martinez. Renewables 2022, analysis and forecast to 2027. Technical report, International Energy Agency, 2022.

[3] Aidong Yang Anton Firth, Bo Zhang. Quantification of global waste heat and its environmental effects. In *Applied Energy*, 2019.

[4] International Renewable Energy Agency. Innovation outlook, thermal energy storage. Technical report, 2020.

[5] L. Miró A.I. Fernández C. Barreneche L.F. Cabeza, I. Martorell. 1-introduction to thermal energy storage (tes) systems. In *Advances in Thermal Energy Storage Systems*, 2015.

[6] Laurent Zalewski Mickael Pailha Maxime Thonon, Gilles Fraisse. Simultaneous charging and discharging processes in latent heat thermal energy storage: A review. In *Thermal Science and Engineering Progress*, 2024.

[7] Christopher Chintua Enweremadu Luckywell Seyitini, Basim Belgasim. Solid state sensible heat storage technology for industrial applications – a review. In *Journal of Energy Storage*, 2023.

[8] Rao Martand Singh Habibollah Sadeghi, Ramin Jalali. A review of borehole thermal energy storage and its integration into district heating systems. In *Renewable and Sustainable Energy Reviews*, 2024.

[9] Navid Khordehgaha Darem Ahmada Tom Lipinskib Hussam Jouharaa, Alina Zabnienska-Gora. Latent thermal energy storage technologies and applications: A review. In *International Journal of Thermofluids*, 2020.

[10] Abdulkafi Mohammed Saeed Kamel Guedri Abed Mourad Obai Younis Thongchai Botmart Sameh Ahmed, Aissa Abderrahmane and Nehad Ali Shah. Melting enhancement of pcm in a finned tube latent heat thermal energy storage. In *Nature*, 2022.

[11] Ji Li Yang Liu, Ruowei Zheng. High latent heat phase change materials (pcms) with low melting temperature for thermal management and storage of electronic devices and power batteries: Critical review. In *Renewable and Sustainable Energy Reviews*, 2022.

[12] Hossein Shokouhmand Babak Kamkari. Experimental investigation of phase change material melting in rectangular enclosures with horizontal partial fins. In *International Journal of Heat and Mass Transfer*, 2014.

[13] P. Muthukumar Muhammad Mustafizur Rahman Fenil Desai, Sunku Prasad Jenneb. Thermochemical energy storage system for cooling and process heating applications: A review. In *Energy Conversion and Management*, 2021.

[14] Marc A. Rosen Ali Haji Abedin. Assessment of a closed thermochemical energy storage using energy and exergy methods. In *Applied Energy*, 2012.

[15] Ingrid Stobera Philipp Blum Paul Fleuchaus, Bas Godschalkb. Worldwide application of aquifer thermal energy storage– a review. In *Renewable and Sustainable Energy Reviews*, 2018.

[16] Vinicius R.B. Boninia Rodrigo Escobar Matías Castro-Quijadab Álvaro Videla Allan R. Starkea, José M. Cardemil. Assessing the performance of novel molten salt mixtureson csp applications. In *Applied Energy*, 2024.

[17] Harald Mehling. Estimation of the worldwide installed capacity of cold storage with ice and its effect in the electricity grid. In *The 13th International Conference on Energy Storage*, 2015.

[18] Thomas Haussmann Harald Mehling, Michael Brütting. Pcm products and their fields of application - an overview of the state in 2020/2021. In *Journal of Energy Storage*, 2022.

[19] L. Luo K.E. N'Tsoukpoe, N. Le Pierrès. Experimentation of a libreh2o absorption process for long-term solar thermal storage: Prototype design and first results. In *Energy*, 2013.

[20] R.Z. Wang Abel Mehari, Z.Y. Xu. Thermal energy storage using absorption cycle and system: A comprehensive review. In *Energy Conversion and Management*, 2020.

[21] Zhiyu Luo Kejin Wang Surendra P. Shah Xiaonan Wang, Wengui Li. A critical review on phase change materials (pcm) for sustainable and energy efficient building: Design, characteristic, performance and application. In *Energy Buildings*, 2022.

[22] Kaia Eichler Per Löveryd Pär Johanssona Angela Sasic Kalagasidisa Pepe Tan, Patrik Lindberg. Effect of phase separation and supercooling on the storage capacity in a commercial latent heat thermal energy storage: Experimental cycling of a salt hydrate pcm. In *Journal of Energy Storage*, 2020.

[23] Amy M. Marconnet Piyush Mani Tripathi. A new thermal management figure of merit for design of thermal energy storage with phase change materials. In *International Journal of Heat and Mass Transfer*, 2024.

[24] Avinash M. Pawar Shivaji K. Maknikar. Application of phase change material (pcm) in battery thermal management system (btms): A critical review. In *Materials Today: Proceedings*, 2023.

[25] Victor J. Ferreira Tatiana García-Armingol Ana M. Lopez-Sabiron German Ferreira Patricia Royo, Luis Acevedo. High-temperature pcm-based thermal energy storage for industrial furnaces installed in energy-intensive industries. In *Energy*, 2019.

[26] Y. Tian C.Y. Zhao, W. Lu. Heat transfer enhancement for thermal energy storage using metal foams embedded within phase change materials (pcms). In *Solar Energy*, 2010.

[27] Jin Du Yue Zhang Ping Ping Xinyi Dai, Depeng Kong. Investigation on effect of phase change material on the thermal runaway of lithium-ion battery and exploration of flame retardancy improvement. In *Process Safety and Environmental Protection*, 2022.

[28] Wang Zhan Yin Chen Mingyi Chen Yuqi Wang, Luyao Zhao. Flame retardant composite phase change materials with mxene for lithium-ion battery thermal management systems. In *Journal of Energy Storage*, 2024.

[29] Rui Yang Ling Xu, Jianping Wang. A new flame retardance strategy for shape stabilized phase change materials by surface coating. In *Solar Energy Materials and Solar Cells*, 2017.

[30] Chuyue Cai Shao Lin Xiaoming Fang Zhengguo Zhang Ziye Ling, Suimin Li. Battery thermal management based on multiscale encapsulated inorganic phase change material of high stability. In *Applied Thermal Engineering*, 2021.

[31] Yingzi Yang Yushi Liu. Preparation and thermal properties of na2co310h2o-na2hpo412h2o eutectic hydrate salt as a novel phase change material for energy storage. In *Applied Thermal Engineering*, 2017.

[32] Andrzej Poniewierski Robert Hołyst. *Thermodynamics for Chemists, Physicists and Engineers*, chapter 8.Phase equilibrium in ideal mixtures. Springer, 2012.

[33] Chamil Abeykoon Yongcai Huang, Alex Stonehouse. Encapsulation methods for phase change materials –a critical review. In *International Journal of Heat and Mass Transfer*, 2023.

[34] Reinhard Radermacher Ho-Hwan Chun Gang Li, Yunho Hwang a. Review of cold storage materials for subzero applications. In *Energy*, 2013.

[35] Bakytzhan Akhmetov Antoni Gil-Jun Onn Khor Anabel Palacios-Yongliang Li Yulong Ding Luisa F. Cabeza Wooi Leong Tan Alessandro Romagnoli Lizhong Yang, Uver Villalobos. A comprehensive review on sub-zero temperature cold thermal energy storage materials, technologies, and applications: State of the art and recent developments. In *Applied Energy*, 2021.

[36] Philip Eames Jose Pereira da Cunha. Thermal energy storage for low and medium temperature applications using phase change materials – a review. In *Applied Energy*, 2016.

[37] Luisa F. Cabeza Harald Mehling. *Heat and cold storage with PCM. An up to date introduction into basics and applications.*, chapter Chapter 2: Solid-liquid phase change materials. Springer, 2008.

[38] M. k. Akacl. J. Stefan. Über einige probleme der theorie der wärmeleitung. In *Acad. Mat. Natur.*, 1889.

[39] V. R. Voller. Fast implicit finite-difference method for the analysis of phase change problems. In *Civil, Environmental, and Geo- Engineering*, 1990.

[40] Juan Du Si-Min Huang Yuxiang Hong, Wei-Biao Ye. Solid-liquid phase-change thermal storage and release behaviors in a rectangular cavity under the impacts of mushy region and low gravity. In *International Journal of Heat and Mass Transfer*, 2019.

[41] Philip C. Eames Mohamed Fadl. Numerical investigation of the influence of mushy zone parameter amush on heat transfer characteristics in vertically and horizontally oriented thermal energy storage systems. In *Applied Thermal Engineering*, 2019.

[42] Fengwu Bai Tiejun Zhang-Zhifeng Wang Bei Yang, Aikifa Raza. Microstructural evolution within mushy zone during paraffin's melting and solidification. In *International Journal of Heat and Mass Transfer*, 2019.

[43] G. Ziskind Y. Kozak. Novel enthalpy method for modeling of pcm melting accompanied by sinking of the solid phase. In *International Journal of Heat and Mass Transfer*, 2017.

[44] R. Hayat G. Ziskind T. Rozenfeld, Y. Kozak. Close-contact melting in a horizontal cylindrical enclosure with longitudinal plate fins: Demonstration, modeling and application to thermal storage. In *International Journal of Heat and Mass Transfer*, 2015.

[45] Hamidreza Rastan Amir Abdi. Experimental comparative analysis of close-contact and constrained melting of n-eicosane in a finned rectangular cavity. In *Applied Thermal Engineering*, 2023.

[46] Zhigao Sun Jun Li Zhipei Hu, Shuo Jiang. Numerical simulation of fin arrangements on the melting process of pcm in a rectangular unit. In *Renewable Energy*, 2024.

[47] Davood D. Ganji-Emmanuel C. Nsofor Jasim M. Mahdi, Sina Lohrasbi. Accelerated melting of pcm in energy storage systems via novel configuration of fins in the triplex-tube heat exchanger. In *International Journal of Heat and Mass Transfer*, 2018.

[48] K. Sopian-M.Y. Sulaiman Abdulrahman Th Mohammad Sohif Mat, Abduljalil A. Al-Abidi. Enhance heat transfer for pcm melting in triplex tube with internal–external fins. In *Energy Conversion and Management*, 2013.

[49] V. Verda A. Sciacovelli, F. Gagliardi. Maximization of performance of a pcm latent heat storage system with innovative fins. In *Applied Energy*, 2015.

[50] Ionatan Anton Schroer Rejane De Césaro Oliveski, Alexandre de Quadro Tacques Filho. Melting and solidification in thermal storage: Influence of fin aspect ratio and positioning in a full charging and discharging cycle. In *Journal of Energy Storage*, 2022.

[51] Patrick J.Shamberger. Cooling capacity figure of merit for phase change materials. In *ASME Journal of Heat and Mass Transfer*, 2016.

[52] Andreas König-Haagen Stephan Höhlein Gonzalo Diarce Ana Lazaro, Monica Delgado. Technical performance assessment of phase change material components. In *IEA SHC International Conference on Solar Heating and Cooling for Buildings and Industry*, 2019.

[53] Dominic Groulx Florent Herbinger. Experimental comparative analysis of finned-tube pcm-heat exchangers' performance. In *Applied Thermal Engineering*, 2022.

[54] Yaohua Zhao-Chuanqi Chen Tengyue Wang Lin Liang Zeyu Wang, Yanhua Diao. Visualization experiment and numerical study of latent heat storage unit using micro-heat pipe arrays: Melting process. In *Energy*, 2022.

[55] Wei Yu Liuwei Wang, Ankang Kan. Melting behavior and heat transfer performance in a modified pcm-filled enclosure with fins under hypergravity conditions. In *International Communications in Heat and Mass Transfer*, 2022.

[56] Qingsong Bai-Qunli Zhang Liwen Jin Jinyue Yan Xiaohu Yang, Zhao Lu. Thermal performance of a shell-and-tube latent heat thermal energy storage unit: Role of annular fins. In *Applied Energy*, 2017.

[57] Xiande He Zhuqian Zhang. Three-dimensional numerical study on solid-liquid phase change within open-celled aluminum foam with porosity gradient. In *Applied Thermal Engineering*, 2017.

[58] J. L. Zeng Z. Cao D. W. Yang L. X. Sun L. Zhang. Thermal conductivity enhancement of ag nanowires on an organic phase change material. In *Journal of Thermal Analysis and Calorimetry*, 2010.

[59] Rouhollah Ahmadi Vahid Piroozmand. Enhancement of pcms performance using nano-particles in horizontal triple-series shell-and-tube heat exchangers: A numerical study. In *Journal of Energy Storage*, 2024.

[60] Sandip K. Sahab Opeyemi A. Abassc Aayush Sharma-Ganesh Balasubramanian Srilok Srinivasan, Mouhamad S. Diallo. Effect of temperature and graphite particle fillers on thermal conductivity and viscosity of phase change material n-eicosane. In *International Journal of Heat and Mass Transfer*, 2017.

[61] Besir Kok. Examining effects of special heat transfer fins designed for the melting process of pcm and nano-pcm. In *Applied Thermal Engineering*, 2020.

[62] Miraç Kan Hasan Karabay Müslüm Arıcı, Ensar Tütüncü. Melting of nanoparticle-enhanced paraffin wax in a rectangular enclosure with partially active walls. In *International Journal of Heat and Mass Transfer*, 2017.

[63] Majid Siavashib Mohammad Mahdi Heyhata, Sepehr Mousavib. Battery thermal management with thermal energy storage composites of pcm, metal foam, fin and nanoparticle. In *Journal of Energy Storage*, 2020.

[64] Hong Wang Xian-Yan He Yu Tan Bin Ding, Xun Zhu. Experimental study on phase change heat transfer characteristics of alloys. In *International Journal of Heat and Mass Transfer*, 2017.

[65] Pengda Li Guoliang Yu Chao Xu Dalang Jiang, Zhirong Liao. The evolution of the mushy zone during the melting process of a binary nitrate salt. In *International Journal of Heat and Mass Transfer*, 2019.

[66] Beasley Donald E. Figliola Richard S. *Theory and design for mechanical measurements*, chapter 5. Uncertainty analysis. Wiley, 2015.

[67] Marc Martin Luisa F. Cabeza, Gabriel Zsembinszki. Evaluation of volume change in phase change materials during their phase transition. In *Journal of Energy Storage*, 2020.

[68] Yang Li Xinghong Luo, Yaya Wang. Role of hydrostatic pressure and wall effect in solidification of tc8 alloy. In *Nature*, 2019.

Appendix A

Thermocouples calibration

The ten thermocouples, four of them N-type and six of them T-type, where calibrated using an ice bath, as shown in Figure A.1. For each thermocouple, five samples of 100 datapoints were obtained, by placing the thermocouples for 1-2 minutes in the ice bath, removing them, and then placing them again in the ice bath in a new position.

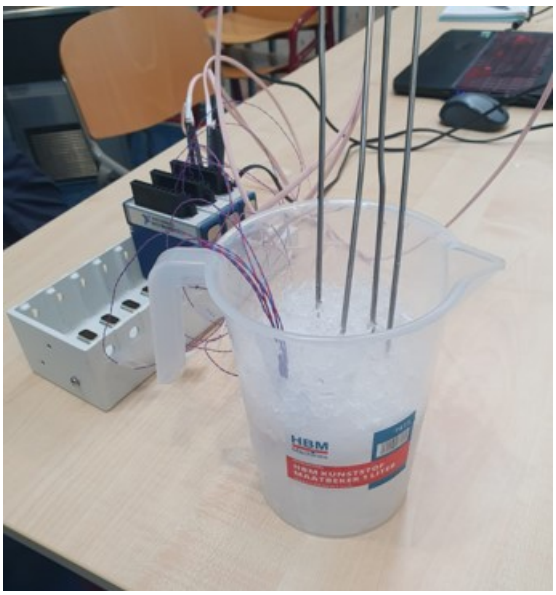

Figure A.1: Bucket filled with ice and thermocouples.

The datapoints collected for each sample are shown in Figure A.2 for the different thermocouples. Additionally, the mean and standard deviation for each sample are summarized in Tables 1 and 2.

Sample #	**N01**	**N02**	**N03**	**N04**	**T01**	**T02**	**T03**	**T04**	**T05**	**T06**
1	0.315	0.283	0.375	0.470	-0.322	-0.197	-0.127	0.019	-0.024	-0.151
2	0.324	0.272	0.355	0.443	-0.307	-0.202	-0.130	0.007	-0.022	-0.124
3	0.306	0.342	0.341	0.428	-0.317	-0.210	-0.161	-0.026	-0.039	-0.171
4	0.310	0.263	0.334	0.412	-0.298	-0.206	-0.162	-0.033	-0.034	-0.157
5	0.325	0.268	0.331	0.418	-0.304	-0.207	-0.163	-0.053	-0.032	-0.157

Table A.1: Mean of the temperature, in celcius degrees, for the different samples and thermocouples submerged in the ice bath.

Sample #	T01	T02	T03	T04	T05	T06	T07	T08	T09	T10
1	0.0449	0.0498	0.0569	0.0546	0.0319	0.0425	0.0512	0.0557	0.0324	0.0325
2	0.0381	0.0401	0.0455	0.0430	0.0324	0.0399	0.0446	0.0490	0.0316	0.0340
3	0.0378	0.0330	0.0406	0.0454	0.0321	0.0359	0.0428	0.0457	0.0239	0.0288
4	0.0372	0.0352	0.0397	0.0419	0.0293	0.0387	0.0394	0.0429	0.0314	0.0314
5	0.0366	0.0362	0.0389	0.0386	0.0279	0.0341	0.0399	0.0443	0.0236	0.0261

Table A.2: Standard deviation, in celcius degrees, for the different thermocouples submerged in the ice bath.

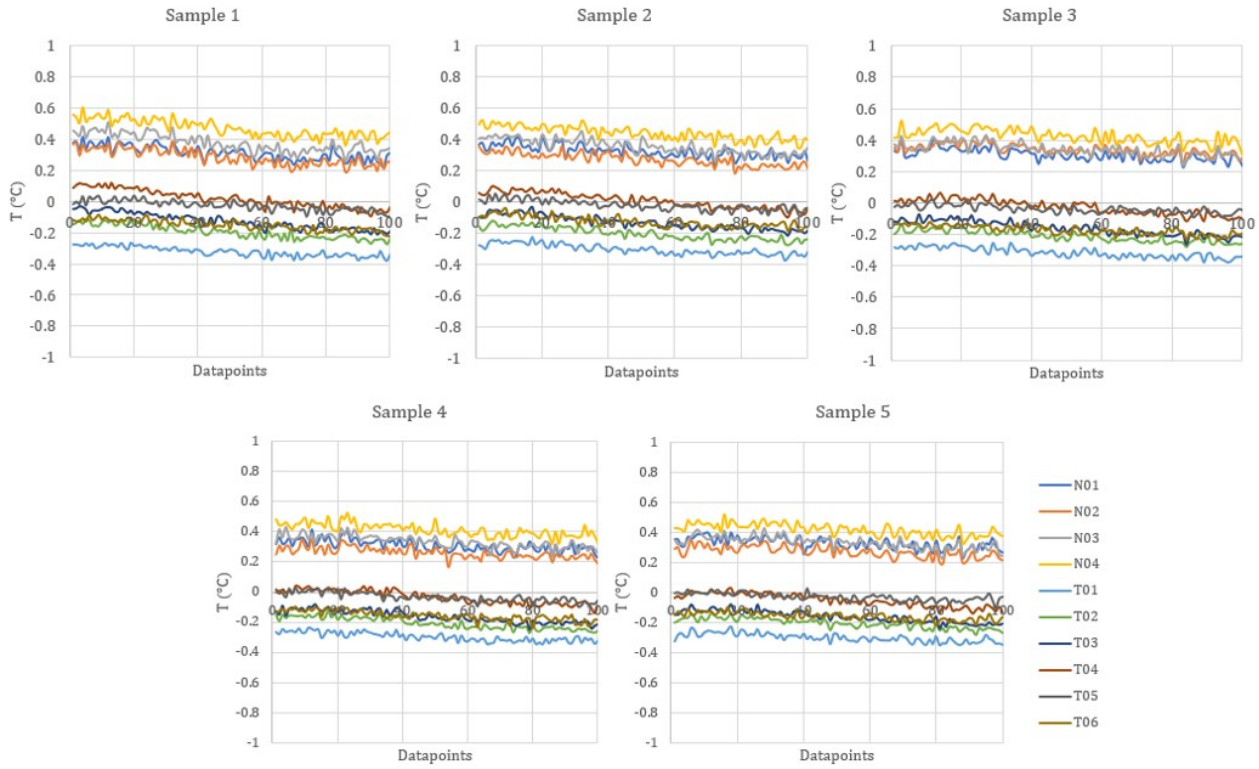

Figure A.2: Bucket filled with ice and thermocouples.

Appendix B

Fluent user-defined-functions

This section presents the code used in the user-defined-function, consisting in two fluent macros, DEFINE_EXECUTE_AT_END, used to get the y-coordinate for the liquid-solid interface at the end of each time step, and DEFINE_PROPERTY, used to define the thermal conductivity of the PCM a a function of temperature and cell centroid.

Listing B.1: Fluent UDF Code

```
#include "udf.h"

#define INTERFACE_TEMP 298.15
#define INITIAL_LOWER_BOUND 0.045     % h_TCO
#define INITIAL_UPPER_BOUND 0.05      % h_PCM
#define INTERFACE_RANGE 0.005

real interface_y = -1;

// Function to update interface_y at every time step
DEFINE_EXECUTE_AT_END(track_interface)
{
    Domain *d;
    Thread *t;
    cell_t c;
    real y[ND_ND];
    real temp;
    real new_interface_y_local = -1;

    d = Get_Domain(1);  // Domain ID
    thread_loop_c(t,d)
    {
        begin_c_loop(c,t)
        {
            C_CENTROID(y,c,t);  // Get cell centroid
            liqF = C_LIQF(c,t);
            if (liqF < 1)
            {
                if (y[1] > new_interface_y_local)
                {
                    new_interface_y_local = y[1];
                }
            }
        }
        end_c_loop(c,t)
    }

    // Reduce local minimums to find global maximum using Fluent's reduction function
    real new_interface_y_global = PRF_GRHIGH1(new_interface_y_local);
```

```
    // Only update and print interface_y if a valid new_interface_y was found
    if (new_interface_y_global < INITIAL_LOWER_BOUND)
    {
        interface_y = new_interface_y_global;

        if (myid == 0)
        {
          Message("Interface position (interface_y) updated to: %f\n", interface_y);
        }
    }
    else
    {
      if (myid == 0)
      {
        Message("No interface found in this time step.\n");
      }
    }
}

// Property UDF to set thermal conductivity based on interface_y
DEFINE_PROPERTY(cell_conductivity, c, t)
{
    const real T_l = 301.15;  // Liquidus temperature
    const real T_s = 298.15;  // Solidus temperature
    real temp = C_T(c, t);
    real mu_k;
    real xyz[ND_ND];  // Array to hold cell centroid coordinates

    C_CENTROID(xyz, c, t);

    // Check if y-coordinate is within the initial range or updated interface range
    if ((interface_y == -1 && xyz[1] >=
    INITIAL_LOWER_BOUND && xyz[1] <= INITIAL_UPPER_BOUND) ||
        (interface_y != -1 && xyz[1] >= interface_y && xyz[1] <=
        interface_y + INTERFACE_RANGE))
    {
        mu_k = 20.22;
    }
    else if (interface_y != -1 && xyz[1] > interface_y + INTERFACE_RANGE)
    {
        // Beyond interface_y + 0.005, set conductivity according to temperature
        if (temp >= T_l)
        {
            mu_k = 0.172;
        }
        else if (temp <= T_s)
        {
            mu_k = 0.293;
        }
        else
        {
            mu_k = 0.293 - (temp - T_s) * 0.121 / (T_l - T_s);
        }
    }
    else
    {
        // If none of the above conditions are met, follow the temperature-based logic
        if (temp >= T_l)
```

```
        {
            mu_k = 0.172;
        }
        else if (temp <= T_s)
        {
            mu_k = 0.293;
        }
        else
        {
            mu_k = 0.293 - (temp - T_s) * 0.121 / (T_l - T_s);
        }
    }
    return mu_k;
}
```